MODELING OF ELASTIC WAVE PROPAGATION IN A FLUID-FILLED BOREHOLE EXCITED BY A PIEZOELECTRIC TRANSDUCER

by

Sergio Kostek[1]

Earth Resources Laboratory
Department of Earth, Atmospheric, and Planetary Sciences
Massachusetts Institute of Technology
Cambridge, MA 02139

ABSTRACT

Acoustic logging is an important geophysical method for obtaining relevant information concerning rock properties in formations traversed by boreholes. Typically, the formation parameters that are measured are the compressional, shear, and Stoneley wave slownesses, which are related to important petrophysical parameters such as porosity, permeability, etc. Theoretical waveform modeling has played an important role in helping to understand the complex wave pattern setup in the borehole, and many processing algorithms have come out of this improved understanding. However, in the presence of formation inhomogeneities and borehole irregularities, which are the most common situations found in practice, no satisfactory modeling scheme has yet been presented. Furthermore, source and receivers have been treated as idealized pointwise transducers, with isotropic radiation patterns. As new applications of full waveform acoustic logs arise, such as sonic imaging, cross-well tomography, etc., a better understanding of the wave phenomena including excitation, propagation, scattering, and detection is necessary for inverting the recorded wavefield. In this paper a velocity-stress finite-difference model is presented for a cylindrical piezoelectric transducer in a borehole. The transducer may be free-flooded or capped, and a variety of support and auxilliary structures may be included. The borehole may be irregular and the surrounding formation inhomogeneous. The model is two-dimensional in that azimuthal symmetry is assumed. The description of the tranducer is a full elasto-electromagnetic one, including transverse isotropy in the elastic, dielectric, and piezoelectric parameters, and dissipation in the piezoelectric material. The borehole propagation portion of the model is verified by comparison with a standard transform technique. Predictions of the model for a piezoelectric cylinder radiating into a fluid medium are compared to experimental results with excellent agreement. The radiation patterns of a bare transducer near resonance frequencies are quite anisotropic. Acoustic waveforms in a borehole excited by a finite

---

[1] On leave from Schlumberger-Doll Research, Old Quarry Road, Ridgefield, CT 06877-4108.

sized cylindrical transducer are displayed and are quite different from those excited by an ideal point pressure source. The effect of borehole loading upon the impedance of the transducer is shown to be small.

INTRODUCTION

Full waveform acoustic logging is a very important geophysical technique used to acquire information from formations traversed by boreholes. Typically, an acoustic source and an array of receivers are deployed along the axis of a fluid-filled borehole, and the receiver responses to an acoustic pulse emitted by the source are digitized and sent uphole through a wireline. On the surface, the receiver signals are processed to extract the compressional, shear, and Stoneley wave slownesses as functions of depth. These measurements are used extensively in evaluating petrophysical parameters of interest such as porosity and permeability, as well as in lithology determination and overpressure detection. Seismic applications of acoustic logs consist mainly of travel time-depth conversion and the construction of synthetic seismograms. Other applications are in hydraulic fracturing and cement bond evaluation in cased holes.

The acoustic wave propagation in a fluid-filled borehole is extremely complex due to the presence of both head waves, trapped fluid modes, and surface waves. A typical waveform consists of overlapping combinations of these waves. Biot (1952) was the first one to study the mode dispersion in a fluid-filled borehole with a homogeneous formation. The work was new and went far to illuminate the properties of the wave propagation mechanism. Synthetic waveforms were first computed by White and Zechman (1968), also assuming a cylindrical borehole and a homogeneous formation. Rosenbaum (1974) studied the case where the formation consisted of a fluid saturated poroelastic solid. His work focussed on the effects of permeability on the various guided phases. Tsang and Rader (1979) implemented an effective method, which they called real axis integration (RAI), to compute the full acoustic response. Also, they carried out branch cut integrations to evaluate the first compressional and shear/pseudo-Rayleigh arrivals individually. Cheng and Toksöz (1981) analysed propagation and dispersion characteristics of guided waves using dispersion curves and synthetic microseismograms. They also studied the effects of a simple tool model consisting of an elastic cylinder centered in the axis of the borehole. Transverse isotropy in the elastic parameters was studied by White and Tongtaow (1981) and later by Chan and Tsang (1983), motivated by the fact that fine layering in sedimentary rocks manifests itself as making the medium transversely isotropic, possessing an axis of symmetry perpendicular to the layering. A definitive study of the space-time dependence of modal propagation in a borehole was presented by Schoenberg et al. (1981). They used theoretical and experimental data from a scale laboratory model, and obtained good agreement between the two techniques for both modal dispersion and mode cutoff frequencies. A general formalism for cylindrically layered media was also presented in that work. The effects of the presence of casing and cement in the borehole were studied by Tubman et al. (1984), using a Thomson-Haskell type propagator matrix.

The aforesaid references dealt primarily with the case of a perfectly cylindrical fluid-filled borehole in either a homogeneous or cylindrically layered formation. Inhomogeneities along the axial direction were first studied by Stephen et al. (1985), who approached the problem by numerically solving the second-order elastic wave equations formulated in terms of the displacements. An explicit finite-difference (FD) scheme was used for that purpose, together with some simple absorbing boundary conditions. The particular formulation they used significantly constrained the spatial variations of the elastic properties of the medium. Also, the continuity conditions at a fluid-solid interface had to be imposed explicitly, limiting the applications to virtually cylindrical boreholes. Qualitative agreement was obtained between waveforms generated with this technique and the discrete wavenumber method (DW). The fundamental problem of a pulsed point source in a fluid-filled borehole with a horizontal bed boundary separating two solid formations was studied by Tsang (1987) using a hybrid method, originally applied to electromagnetic induction logging (Chew et al., 1984). The essence of the method consisted in converting the compressional and shear head wave branch-cut contributions into discrete modes, by introducing a stress-free boundary far away from the borehole. These discrete modes, together with the normal modes and the Stoneley mode, formed a basis for the solution. The boundary conditions at the horizontal interface coupled the modes in the two solid regions. Numerical computations were performed only up to the beginning of the Stoneley mode arrivals, since late arrivals would have required extensive computational time. An interesting approach for the computation of the elastodynamic body-wave field outside a fluid-filled borehole has been recently developed (Ben-Menahem and Kostek, 1990), whereby the far-field effects of the borehole are replaced by an equivalent force system. This is relevant for the interpretation of cross-well tomographic data.

A common point to all these previous works is that they concentrated mostly on the propagation phenomena, with little or no account of the excitation and detection of the borehole signals. In acoustic well logging the source of acoustic waves is typically a free-flooded piezoelectric cylinder, which is well suited for broadband applications. The broad band characteristics stem from the open-pipe resonance of the fluid within the cylinder. Relatively little work has been done on the coupled transducer-fluid problem. In the context of well logging no solution has been presented to date, which accounts for the coupling of the transducer, borehole fluid, and formation. Since the behaviour of the transducer is strongly influenced by the acoustic loading due to the cavity resonance and since the transducer is quadrupole in nature, the problem cannot be approached by simple lumped-element analysis. Haskins and Walsh (1957) derived expressions for the *in vacuum* mechanical vibrations of a ferroelectric tube having transverse isotropy, assuming that the electric field was uncoupled from the elastodynamic field. This was later modified by Drumheller and Kalnins (1969), who presented a coupled elasto-electromagnetic thin shell theory. They found differences between the coupled and uncoupled analyses for modes of vibrations which involved significant bending of the shell. Wilkinson and DaCosta (1971) studied the radiation problem of a free-flooded piezoelectric cylinder polarized circumferentially. The radiation part was handled by spreading a sheet of acoustic sources over the surface of the shell in contact with the fluid, and adjusting the magnitude of the source strengths so that the boundary conditions at the surface were satisfied. Smith et al. (1973) used a finite element technique to model the elastic response, whereas the acoustic radiation loading on the transducer was modeled by approximating the surface Helmholtz integral equation for the fluid medium. This formulation was further improved by Hunt et al. (1974), who obtained a more accurate representation of the near-field pressure. An approximate theory for low frequency radiation was used by Zalesak and Rogers (1974) to study radially, circumferentially, and axially polarized rings operating below resonance. Rogers (1986) developed a model for the transmitting response and electrical impedance of a free-flooded, thickness-polarized piezoelectric cylinder transducer. The elasticity of the cylinder was described using membrane theory modified to account for piezoelectric effects. The complete solution for the vibration of the cylinder was found in the form of a sum of the particular solution and the normal modes appropriate to a non-piezoelectric cylinder with free ends.

As new and more demanding applications of full waveform acoustic logs arise, for example cross-well tomography, a better understanding of the wave phenomena including excitation, propagation, scattering, and detection is necessary for inverting the recorded wavefield. In view of all the present limitations, a finite-difference modeling scheme based on a velocity-stress formulation of the elastodynamic equations is presented in this paper, which is able to accurately model wave propagation phenomena in irregular boreholes surrounded by formations with radial and axial dependence of the elastic parameters. The source (transducer) is modeled as a fully coupled piezoelectric element exhibiting transverse isotropy in the elastic, dielectric, and piezoelectric parameters. Since most piezoelectric materials exhibit mechanical dissipation, a time-domain constant Q model for the transducer is also presented in this work. Results of simulations for the pure elastodynamic borehole problem are presented and compared to waveforms generated by the RAI method. To validate the theoretical transducer model, a series of simulations were carried out and compared with experimental results (Chiou, 1989). In the next section we present the basic governing equations as well as all the approximations involved. The numerical implementations are then presented. The results of simulations and comparisons with experimental results follows. A further addition to this borehole modeling scheme has recently been implemented (Kostek and Randall, 1990), enabling the inclusion of a single or multiple horizontal fractures intersecting the borehole.

THEORETICAL FORMULATION

The basic conservation equations and constitutive relations governing the dynamic behaviour of elastic and piezoelectric media are introduced in this section. A constant Q model to account for mechanical dissipation in the piezoelectric medium is also discussed.

Elastic Wave Propagation

In a linear isotropic elastic medium the particle velocity vector $\mathbf{v}$ and the stress tensor $\boldsymbol{\tau}$ satisfy the following first-order hyperbolic system of equations

$$\rho\frac{\partial \mathbf{v}}{\partial t} = \nabla\cdot\boldsymbol{\tau}, \qquad (1)$$

$$\frac{\partial \boldsymbol{\tau}}{\partial t} = \lambda(\nabla\cdot\mathbf{v})\mathbf{I}+\mu(\nabla\mathbf{v}+\mathbf{v}\nabla), \qquad (2)$$

where $\mathbf{I}$ is the second-rank identity tensor, ρ is the volume density of mass, and λ, μ are the Lamé parameters of the medium. Eq. (1) simply states the balance of linear momentum and Eq. (2) is the constitutive relation for the elastic material composing the medium. The field variables $(\mathbf{v},\boldsymbol{\tau})$ have both spatial and temporal dependences, whereas the elastic parameters (ρ,λ,μ) exhibit only spatial dependence. In cylindrical coordinates, Eqs. (1) and (2) are written in their component form as

$$\rho\frac{\partial v_r}{\partial t} = \frac{1}{r}\frac{\partial}{\partial r}(r\tau_{rr})-\frac{\tau_{\theta\theta}}{r}+\frac{\partial\tau_{rz}}{\partial z}, \qquad (3)$$

$$\rho\frac{\partial v_z}{\partial t} = \frac{1}{r}\frac{\partial}{\partial r}(r\tau_{rz})+\frac{\partial\tau_{zz}}{\partial z}, \qquad (4)$$

$$\frac{\partial\tau_{rr}}{\partial t} = \lambda\left(\frac{1}{r}\frac{\partial}{\partial r}(rv_r)+\frac{\partial v_z}{\partial z}\right)+2\mu\frac{\partial v_r}{\partial r}, \qquad (5)$$

$$\frac{\partial\tau_{\theta\theta}}{\partial t} = \lambda\left(\frac{1}{r}\frac{\partial}{\partial r}(rv_r)+\frac{\partial v_z}{\partial z}\right)+2\mu\frac{v_r}{r}, \qquad (6)$$

$$\frac{\partial\tau_{zz}}{\partial t} = \lambda\left(\frac{1}{r}\frac{\partial}{\partial r}(rv_r)+\frac{\partial v_z}{\partial z}\right)+2\mu\frac{\partial v_z}{\partial z}, \qquad (7)$$

$$\frac{\partial\tau_{rz}}{\partial t} = \mu\left(\frac{\partial v_z}{\partial r}+\frac{\partial v_r}{\partial z}\right). \qquad (8)$$

The reason for using this particular formulation instead of the second-order displacement formulation, is due to the fact that, once discretized, the stability condition and the

P-wave velocity dispersion curve do not depend on the Poisson's ratio, while the S-wave phase velocity dispersion curve behaviour is rather insensitive to the Poisson's ratio (Virieux, 1986). This allows the modeling of fluid media by setting the shear rigidity to zero. Hence, these boundaries may be of arbitrary shape, without incurring unreasonable programming logic.

Transducer Modeling

Most acoustic transducers (transmitters or receivers) are made of piezoelectric materials. The direct piezoelectric effect is the property that some bodies have of becoming electrically charged under mechanical stresses (see Figure 1). This behaviour which is spontaneous in several natural or man made crystals such as quartz or Rochelle salt, is due to the crystalline structure whereby a mechanical action provokes the appearance of an electric dipole in each crystalline unit cell of material by shifting the centers of the positive and negative charges. The electrostatic balance being broken, polarization occurs. There is a correlative converse effect, an electric field bringing about a mechanical deformation of the material. Piezoelectricity cannot occur in conducting bodies or in those that are highly symmetrical. Actually, the absence of a center of symmetry in the unit cell is a necessary condition for this phenomenon to occur. Some piezoelectric crystals are also ferroelectric; a polarization P corresponds to an exciting electric field E and the curve of P versus E is closed and analogous to the magnetic hysteresis cycle, thus enabling a remanent polarization P_r and a coercive field E_c to be defined. This is particularly so with barium titanate ($BaTiO_3$) and many salts (titanates and zirconates) which similarly possess the crystalline structure of perovskite ($CaTiO_3$).

Ceramics differ from piezoelectric crystals, and their excellent piezoelectric properties are due to the existence of ferroelectricity. By sintering lead, zirconium and titanium oxides or salts, general formulation compounds are made: $PbTi_{1-x}Zr_xO_3$ ($x \approx 0.5$). The nomenclature PZT (lead-zirconate-titanate) stems from the chemical composition. In all these compounds the single microcrystals are ferroelectric, and hence possess spontaneous polarization, but the disordered aggregate of these microcrystals forming the straight sintered ceramic has no total dipole electric moment, on a macroscopic scale. In order to introduce into such a medium the anisotropy needed for piezoelectricity to exist, it must undergo a strong electric field, which by preferentially aligning the single microcrystals along its direction, will induce quite considerable remanent polarisation. It is only after this process that the ceramic becomes ferroelectric and thereby piezoelectric.

The coupled elasto-electromagnetic problem will now be analysed from first principles and the equations which approximate the behaviour of the system will be derived. For our purposes we will assume that the piezoelectric medium behaves linearly, and thus the constitutive relations between the elastodynamic and electric field variables (namely the stress tensor $\boldsymbol{\tau}$, the strain tensor $\boldsymbol{\varepsilon}$, the electric displacement $\mathbf{D}$, and the electric field $\mathbf{E}$), in the absence of magnetic effects, are given by (Auld, 1990)

$$\boldsymbol{\tau} = \mathbf{c}^E : \boldsymbol{\varepsilon} - \mathbf{e} \cdot \mathbf{E}, \tag{9}$$

$$\mathbf{D} = \mathbf{e} : \boldsymbol{\varepsilon} + \boldsymbol{\epsilon}^{\varepsilon} \cdot \mathbf{E}, \tag{10}$$

where $\mathbf{c}^E$ is the fourth-rank elastic stiffness tensor at constant electric field, $\mathbf{e}$ is the third-rank piezoelectric tensor, and $\boldsymbol{\epsilon}^{\varepsilon}$ is the second-rank dielectric permitivity tensor at constant strain. Alternatively, one can also write

$$\mathbf{D} = \boldsymbol{\epsilon}^{\tau} \cdot \mathbf{E} + \mathbf{d} : \boldsymbol{\tau}, \tag{11}$$

$$\boldsymbol{\varepsilon} = \mathbf{d} \cdot \mathbf{E} + \mathbf{s}^E : \boldsymbol{\tau}, \tag{12}$$

where $\mathbf{s}^E$ is the fourth-rank elastic compliance tensor at constant electric field, $\mathbf{d}$ is the third-rank piezoelectric tensor, and $\boldsymbol{\epsilon}^{\tau}$ is the second-rank dielectric tensor at constant stress. The relations between the various coefficients are derived from symmetry considerations and are given in component form as

$$e_{ijk} = d_{ilm} c^E_{lmjk}, \tag{13}$$

$$\epsilon^{\varepsilon}_{ij} = \epsilon^{\tau}_{ij} - d_{ilm} c^E_{lmpq} d_{pqj}, \tag{14}$$

where Einstein's summation convention is implied for repeated indices. The equations of motion as well as Maxwell's equations govern the propagation of waves in such a medium. In invariant notation, these equations are

$$\rho \frac{\partial \mathbf{v}}{\partial t} = \nabla \cdot \boldsymbol{\tau}, \tag{15}$$

$$\rho \frac{\partial \varepsilon}{\partial t} = \frac{1}{2} \left(\nabla \mathbf{v} + \mathbf{v} \nabla \right), \tag{16}$$

$$\nabla \times \mathbf{E} = -\frac{\partial \mathbf{B}}{\partial t}, \tag{17}$$

$$\nabla \times \mathbf{H} = \frac{\partial \mathbf{D}}{\partial t} + \mathbf{J}_c + \mathbf{J}_s, \tag{18}$$

$$\nabla \cdot \mathbf{B} = 0, \tag{19}$$

$$\nabla \cdot \mathbf{D} = \rho_e, \tag{20}$$

where $\mathbf{B}$ and $\mathbf{H}$ are the magnetic induction and magnetic field vectors respectively, $\mathbf{J}_c$ and $\mathbf{J}_s$ are the conduction and source current densities respectively, and ρ_e is the electric charge density. The system (15)-(20) together with the constitutive relations (9)-(10) and

$$\mathbf{B} = \mu_0 \mathbf{H}, \tag{21}$$

where μ_0 is the free-space magnetic permeability, as well as initial and boundary conditions forms the initial boundary-value problem governing the propagation of elasto-electromagnetic waves in a linear piezoelectric medium. Solving these equations is a formidable task since two very different wavelengths are involved, namely the elastic wavelength λ_{el} associated with either compressional or shear waves, and the electromagnetic wavelength λ_{em}. At low enough frequencies, and in particular in the audible range, the effects of piezoelectric coupling between electromagnetic and elastic waves are completely negligible by comparison with the influence of the quasi-static electric field. Consequently, insignificant errors are introduced if the rotational (or electromagnetic) part of $\mathbf{E}$ is neglected. This is called the quasi-static approximation, and it allows us to define an electric potential such that $\mathbf{E} = -\nabla\varphi$. With this approximation our initial boundary-value problem simplifies to

$$\rho\frac{\partial \mathbf{v}}{\partial t} = \nabla\cdot\boldsymbol{\tau}, \tag{22}$$

$$\rho\frac{\partial \boldsymbol{\varepsilon}}{\partial t} = \frac{1}{2}\left(\nabla\mathbf{v} + \mathbf{v}\nabla\right), \tag{23}$$

$$\nabla\cdot\mathbf{D} = \rho_e, \tag{24}$$

$$\boldsymbol{\tau} = \mathbf{c}^E : \boldsymbol{\varepsilon} - \mathbf{e}\cdot\mathbf{E}, \tag{25}$$

$$\mathbf{D} = \mathbf{e} : \boldsymbol{\varepsilon} + \boldsymbol{\epsilon}^{\varepsilon}\cdot\mathbf{E}. \tag{26}$$

Finally, we need to consider the type of crystal symmetry that is present in the PZT materials that we deal with. These materials exhibit hexagonal symmetry and therefore are locally transversely isotropic, being characterized by five elastic constants, three piezoelectric constants and two dielectric constants. We use the following isomorphism to map out all fourth- and third-rank tensors into second-rank tensors

$$\begin{aligned}(11) &\rightarrow (1)\\ (22) &\rightarrow (2)\\ (33) &\rightarrow (3)\\ (23) &\rightarrow (4)\end{aligned}$$

$$(13) \rightarrow (5)$$
$$(12) \rightarrow (6).$$

Obviously, if $(i,j) \rightarrow (m)$ then $(j,i) \rightarrow (m)$. Table 1 shows all the coefficients and how they relate the various fields. Since the problem we are considering has cylindrical symmetry, the following convention for the coordinate axis is used; $\hat{\mathbf{e}}_\theta = \hat{\mathbf{e}}_1$, $\hat{\mathbf{e}}_z = \hat{\mathbf{e}}_2$, $\hat{\mathbf{e}}_r = \hat{\mathbf{e}}_3$, and the direction of polarization is the 3–direction. In this coordinate system, the constitutive relations are written as

$$\frac{\partial \tau_{\theta\theta}}{\partial t} = c_{11}^E \frac{v_r}{r} + c_{12}^E \frac{\partial v_z}{\partial z} + c_{13}^E \frac{\partial v_r}{\partial r} - e_{31}\dot{E}_r, \tag{27}$$

$$\frac{\partial \tau_{zz}}{\partial t} = c_{12}^E \frac{v_r}{r} + c_{11}^E \frac{\partial v_z}{\partial z} + c_{13}^E \frac{\partial v_r}{\partial r} - e_{31}\dot{E}_r, \tag{28}$$

$$\frac{\partial \tau_{rr}}{\partial t} = c_{13}^E \frac{v_r}{r} + c_{13}^E \frac{\partial v_z}{\partial z} + c_{33}^E \frac{\partial v_r}{\partial r} - e_{33}\dot{E}_r, \tag{29}$$

$$\frac{\partial \tau_{rz}}{\partial t} = c_{44}^E \left(\frac{\partial v_r}{\partial z} + \frac{\partial v_z}{\partial r}\right) - e_{15}\dot{E}_z, \tag{30}$$

$$\frac{\partial D_z}{\partial t} = e_{15} \left(\frac{\partial v_r}{\partial z} + \frac{\partial v_z}{\partial r}\right) + \epsilon_{11}^{\epsilon}\dot{E}_z, \tag{31}$$

$$\frac{\partial D_r}{\partial t} = e_{31} \left(\frac{\partial v_z}{\partial z} + \frac{v_r}{r}\right) + e_{33}\frac{\partial v_r}{\partial r} + \epsilon_{33}^{\epsilon}\dot{E}_z, \tag{32}$$

where the dot $(\dot{})$ represents differentiation with respect to the time variable. The absence of free charge ($\rho_e = 0$) inside the piezoelectric medium is expressed by

$$\frac{\partial \dot{D}_r}{\partial r} + \frac{\dot{D}_r}{r} + \frac{\partial \dot{D}_z}{\partial z} = 0. \tag{33}$$

Defining

$$\Delta\tau_{\theta\theta} = c_{11}^E \frac{v_r}{r} + c_{12}^E \frac{\partial v_z}{\partial z} + c_{13}^E \frac{\partial v_r}{\partial r}, \tag{34}$$

$$\Delta\tau_{zz} = c_{12}^E \frac{v_r}{r} + c_{11}^E \frac{\partial v_z}{\partial z} + c_{13}^E \frac{\partial v_r}{\partial r}, \tag{35}$$

$$\Delta\tau_{rr} = c_{13}^E \frac{v_r}{r} + c_{13}^E \frac{\partial v_z}{\partial z} + c_{33}^E \frac{\partial v_r}{\partial r}, \tag{36}$$

$$\Delta\tau_{rz} = c_{44}^E \left(\frac{\partial v_r}{\partial z} + \frac{\partial v_r}{\partial z}\right), \tag{37}$$

it follows that

$$e_{15}\left(\frac{\partial v_r}{\partial z} + \frac{\partial v_r}{\partial z}\right) = d_{15}\Delta\tau_{rz}, \tag{38}$$

$$e_{31}\left(\frac{\partial v_z}{\partial z}+\frac{v_r}{r}\right) = d_{33}\left(\Delta\tau_{\theta\theta}+\Delta\tau_{zz}+\Delta\tau_{rr}\right)-e_{33}\frac{\partial v_r}{\partial r}, \tag{39}$$

where, according to (13)

$$e_{31} = d_{31}\left(c_{11}^E+c_{12}^E\right)+d_{33}c_{13}^E, \tag{40}$$

$$e_{31} = 2d_{31}c_{13}^E+d_{33}c_{13}^E, \tag{41}$$

$$e_{15} = d_{15}c_{44}^E. \tag{42}$$

Combining equations (31)-(32) with (38)-(39) yields

$$\frac{\partial D_z}{\partial t} = d_{15}\Delta\tau_{rz}+\epsilon_{11}^{\varepsilon}\dot{E}_z, \tag{43}$$

$$\frac{\partial D_r}{\partial t} = d_{31}\left(\Delta\tau_{\theta\theta}+\Delta\tau_{zz}\right)+d_{33}\Delta\tau_{rr}+\epsilon_{33}^{\varepsilon}\dot{E}_r. \tag{44}$$

Substituting (43)-(44) into Eq. (33), and using the fact that $\mathbf{E}=-\nabla\varphi$, gives a Poisson equation for the electric potential

$$\epsilon_{33}^{\varepsilon}\left(\frac{\partial^2\dot{\varphi}}{\partial r^2}+\frac{1}{r}\frac{\partial\dot{\varphi}}{\partial r}\right)+\epsilon_{11}^{\varepsilon}\frac{\partial^2\dot{\varphi}}{\partial z^2} =$$

$$\left(\frac{\partial}{\partial r}\frac{1}{r}\right)\left[d_{31}\left(\Delta\tau_{\theta\theta}+\Delta\tau_{zz}\right)+d_{33}\Delta\tau_{rr}\right]+\frac{\partial}{\partial z}\left(d_{15}\Delta\tau_{rz}\right), \tag{45}$$

where the right hand side is the mechanical forcing term. The applied voltage across the thickness of the transducer gives the boundary conditions associated with the above equation. Once the electric potential is known, the electric field and the electric displacement can be computed. The former is required for the calculation of the stresses while the surface integral of the latter yields the electric current flow through the transducer. Equations (3)-(4), (27)-(32), and (45) form a full elasto-electromagnetic model of a lossless piezoelectric transducer. However, many piezoelectric materials exhibit substantial mechnical dissipation. A time domain model for attenuation is discussed next.

Inclusion of Attenuation

The inclusion of a frequency-dependent Q model in time-domain computation is considered here. A generalization of the method used by Emmerich and Korn (1987) to anisotropic elastic media is developed, but for simplicity only the scalar case will be presented. The relation between the stress τ and strain ε in the case of a linear viscoelastic solid is expressed in the frequency as

$$\tau(\omega) = \mathrm{M}(\omega) : \varepsilon(\omega), \tag{46}$$

where $\mathrm{M}(\omega)$ is a complex, frequency dependent viscoelastic tensor. From now on, a scalar version of (46) will be used, where $M(\omega)$ will be just one element of $\mathrm{M}(\omega)$. In the next section, the numerical implementation of the method derived here will be generalized to the case of a constant Q transversely isotropic medium.

Causality implies that the real and imaginary parts of $M(\omega)$ must obey a Kramers-Krönig relation. This means that if we specify the quality factor, defined as

$$Q(\omega) = \frac{\Im\{M(\omega)\}}{\Re\{M(\omega)\}}, \tag{47}$$

the viscoelastic tensor is completely defined. In the time domain, the scalar version of Eq. (46) becomes

$$\tau(t) = \int_{-\infty}^{t} M(t-\xi)\varepsilon(\xi)d\xi. \tag{48}$$

This equation requires an integration over the whole strain history at every point to produce the stress at a particular instant in time. This is very computationally demanding and we will seek better ways to accomplish this. If for instance the complex viscoelastic tensor can be expressed as a rational polynomial in $i\omega$, i.e.,

$$M_L(\omega) = \frac{P_L(i\omega)}{Q_L(i\omega)}, \tag{49}$$

where

$$P_L(i\omega) = \sum_{l=0}^{L} p_l \, (i\omega)^l, \tag{50}$$

$$Q_L(i\omega) = \sum_{l=0}^{L} q_l \, (i\omega)^l, \tag{51}$$

then, the time domain stress-strain relation can be expressed as

$$\sum_{l=0}^{L} q_l \frac{d^l}{dt^l}\tau(t) = \sum_{l=0}^{L} p_l \frac{d^l}{dt^l}\varepsilon(t). \tag{52}$$

This equation can now be solved, for instance, by a finite-difference method.

Introducing the relaxation function $R(t)$, which is the stress response due to a unit step in strain, Eq. (48) yields

$$R(t) = \int_{-\infty}^{t} M(t-\xi)d\xi. \tag{53}$$

From the analyticity of $M(\omega)$ in the upper-half complex ω-plane, we can express $R(t)$ as

$$R(t) = \left[M_r + \delta M \int r(\omega)e^{-\omega t}d\omega\right] H(t), \tag{54}$$

where M_r is the relaxed viscoelastic coefficient, $\delta M = M_u - M_r$ with M_u being the unrelaxed modulus or instantaneous elastic response, $H(t)$ the unit step function, and $r(\omega)$ is the normalized relaxation spectrum with

$$\int_0^\infty r(\omega)d\omega = 1. \tag{55}$$

Eq. (48) can then be written in terms of the relaxation spectrum as

$$\tau(t) = M_u - \delta M \int_{-\infty}^{t}\int_0^\infty \omega\ r(\omega)e^{-\omega(t-\xi)}\varepsilon(\xi)d\omega d\xi. \tag{56}$$

Assuming that the relaxation spectrum consists of L single peaks of strength a_l, at discrete frequencies ω_l

$$r(\omega) = \sum_{l=1}^{L} a_l \delta(\omega - \omega_l), \tag{57}$$

the normalization condition (55) requires that

$$\sum_{l=1}^{L} a_l = 1. \tag{58}$$

This yields

$$M_m(\omega) = M_u - \delta M \sum_{l=1}^{L} \frac{a_l \omega_l}{i\omega + \omega_l}, \tag{59}$$

and the stress-strain relation now becomes

$$\tau(t) = M_u \left[\varepsilon(t) - \sum_{l=1}^{L} \zeta_l(t)\right], \tag{60}$$

where each ζ_l satisfies a first order differential equation

$$\frac{d}{dt}\zeta_l(t) + \omega_l \zeta_l(t) = a_l \omega l \frac{\delta M}{M}\varepsilon(t). \tag{61}$$

Rewriting Eq. (59) as

$$M_m(\omega) = M_r + \sum_{l=1}^{L} a_l \delta M \frac{i\omega}{i\omega + \omega_l}, \tag{62}$$

shows that it can be reinterpreted as the rheological model for a generalized Maxwell body, where each term of the sum is a classical Maxwell body with viscosity $a_l \delta M/\omega_l$ and elastic modulus $a_l \delta M$, and the term M_r represents an additional elastic element. The Q law for this generalized Maxwell body is

$$Q^{-1}(\omega) = \frac{\Im\{M_m\}}{\Re\{M_m\}} = \frac{\delta M}{M_r}\left[\sum_{l=1}^{L} \frac{a_l(\omega/\omega_l)^2}{1+(\omega/\omega_l)^2}\right]\left[1 + \frac{\delta M}{M_r}\sum_{l=1}^{L}\frac{a_l(\omega/\omega_l)^2}{1+(\omega/\omega_l)^2}\right]^{-1}. \tag{63}$$

Assuming that $\delta M \ll M_r$, Eq. (63) can be approximated by

$$Q^{-1}(\omega) \approx \frac{\delta M}{M_r}\sum_{l=1}^{L}\frac{a_l(\omega/\omega_l)^2}{1+(\omega/\omega_l)^2}. \tag{64}$$

This last expression means that Q^{-1} of the generalized Maxwell body is approximately the sum of L Debye functions with maxima $a_l \delta M/2M_r$ located at frequencies ω_l. In Appendix C we show how the coefficients a_l are determined given any Q law. This procedure is much superior to the Padé approximant used by Day and Minster (1984).

NUMERICAL IMPLEMENTATION

In this section, a stable and accurate finite-difference discretization of the equations governing the behaviour of elastic and piezoelectric media is presented. Figure 2 shows the layout of the grid upon the computational domain, and the placement of the various quantities on the grid. The spatial and temporal staggering of the velocity and stresses is necessary in order to have all finite-difference approximations properly centered.

Interior Elastic Equations

Introducing the forward difference operator

$$\delta_r f(r_j) = \delta_r f_j = f_{j+1} - f_j, \tag{65}$$

and the forward average operator

$$\sigma_r f(r_j) = \sigma_r f_j = (f_{j+1} + f_j)/2, \tag{66}$$

with similar definitions for δ_z, δ_t, σ_z, and σ_t, we can write approximations to Eqs. (3)–(8) as (Virieux, 1986)

$$\begin{aligned}\left(\sigma_r \rho_{j-1/2,k+1/2}\right) \frac{\delta_t v^n_{r\ j,k+1/2}}{\Delta t} &= \frac{1}{r_j}\frac{\delta_r \left(r\tau_{rr}^{n+1/2}\right)_{j-1/2,k+1/2}}{\Delta r} - \frac{1}{r_j}\sigma_r \tau^{n+1/2}_{\theta\theta\ j-1/2,k+1/2} \\ &\quad + \frac{\delta_z \tau^{n+1/2}_{rz\ j,k}}{\Delta z},\end{aligned} \tag{67}$$

$$\left(\sigma_z \rho_{j+1/2,k-1/2}\right) \frac{\delta_t v^n_{z\ j+1/2,k}}{\Delta t} = \frac{1}{r_{j+1/2}}\frac{\delta_r \left(r\tau_{rz}^{n+1/2}\right)_{j,k}}{\Delta r} + \frac{\delta_z \tau^{n+1/2}_{zz\ j+1/2,k-1/2}}{\Delta z}, \tag{68}$$

$$\begin{aligned}\frac{\delta_t \tau^{n+1/2}_{\theta\theta\ j+1/2,k+1/2}}{\Delta t} &= \lambda_{j+1/2,k+1/2}\left(\frac{1}{r_{j+1/2}}\frac{\delta_r (r v^n_r)_{j,k+1/2}}{\Delta r} + \frac{\delta_z v^n_{z\ j+1/2,k}}{\Delta z}\right) \\ &\quad + \frac{2\mu_{j+1/2,k+1/2}}{r_{j+1/2}}\sigma_r v^n_{r\ j,k+1/2},\end{aligned} \tag{69}$$

$$\begin{aligned}\frac{\delta_t \tau^{n+1/2}_{zz\ j+1/2,k+1/2}}{\Delta t} &= \lambda_{j+1/2,k+1/2}\left(\frac{1}{r_{j+1/2}}\frac{\delta_r (r v^n_r)_{j,k+1/2}}{\Delta r} + \frac{\delta_z v^n_{z\ j+1/2,k}}{\Delta z}\right) \\ &\quad + 2\mu_{j+1/2,k+1/2}\frac{\delta_z v^n_{z\ j+1/2,k}}{\Delta z},\end{aligned} \tag{70}$$

$$\begin{aligned}\frac{\delta_t \tau^{n+1/2}_{rr\ j+1/2,k+1/2}}{\Delta t} &= \lambda_{j+1/2,k+1/2}\left(\frac{1}{r_{j+1/2}}\frac{\delta_r (r v_r)^n_{j,k+1/2}}{\Delta r} + \frac{\delta_z v^n_{z\ j+1/2,k}}{\Delta z}\right) \\ &\quad + 2\mu_{j+1/2,k+1/2}\frac{\delta_r v^n_{r\ j,k+1/2}}{\Delta r},\end{aligned} \tag{71}$$

$$\begin{aligned}\frac{\delta_t \tau^{n+1/2}_{rz\ j,k}}{\Delta t} &= \left(\sigma^H_r \sigma^H_z \mu_{j-1/2,k-1/2}\right)\left(\frac{\delta_r v^n_{z\ j-1/2,k}}{\Delta r}\right. \\ &\quad \left. + \frac{\delta_z v^n_{r\ j,k-1/2}}{\Delta z}\right),\end{aligned} \tag{72}$$

where the harmonic averaging operator is defined as $\sigma_r^H f(r_j) = [1/2(1/f_{j+1} + 1/f_j)]^{-1}$, and $r_j = j\Delta r$. The reason for using this particular averaging procedure instead of a straight arithmetic average of the elastic properties is that, effectively, the wavelength is much larger than the grid size $\lambda \gg h$, where $h = O(\Delta r) = O(\Delta z)$. In this long wavelength (low frequency) regime, the compliances should be arithmetically averaged rather than the stiffnesses. This problem is analogous to finding the effective elastic constant of a collection of springs connected in series. From this, one also concludes that if the particular point of interest lies on a fluid solid interface, then automatically the effective shear rigidity μ will vanish and the shear stress will also vanish according to Eq. (8). This scheme automatically takes care of irregular fluid-solid interfaces and one does not have to keep track explicitly of the proper boundary conditions.

The stability of this system is guaranteed provided the following relation is satisfied

$$c_{max}\Delta t \left(\frac{1}{\Delta r^2} + \frac{1}{\Delta z^2}\right)^{1/2} < 1, \tag{73}$$

where c_{max} is the maximum P-wave velocity on the grid. The stability condition is independent of both the S-wave velocity and the Poisson's ratio. The scheme is second-order accurate in space and time, and thus $h \leq O(\lambda_{min}/10)$ in order to minimize numerical grid dispersion. Here λ_{min} is the minimum wavelength travelling on the grid.

In a piezoelectric medium (transducer), Eqs. (27)–(30) in the absence of an electric field are approximated by

$$\frac{\delta_t \tau^{n+1/2}_{\theta\theta\ j+1/2,k+1/2}}{\Delta t} = c^E_{11}\frac{\sigma_r v^{n+1}_{r\ j,k+1/2}}{r_{j+1/2}} + c^E_{12}\frac{\delta_z v^{n+1}_{z\ j+1/2,k}}{\Delta z} + c^E_{13}\frac{\delta_r v^{n+1}_{r\ j,k+1/2}}{\Delta r}, \tag{74}$$

$$\frac{\delta_t \tau^{n+1/2}_{zz\ j+1/2,k+1/2}}{\Delta t} = c^E_{12}\frac{\sigma_r v^{n+1}_{r\ j,k+1/2}}{r_{j+1/2}} + c^E_{11}\frac{\delta_z v^{n+1}_{z\ j+1/2,k}}{\Delta z} + c^E_{13}\frac{\delta_r v^{n+1}_{r\ j,k+1/2}}{\Delta r}, \tag{75}$$

$$\frac{\delta_t \tau^{n+1/2}_{rr\ j+1/2,k+1/2}}{\Delta t} = c^E_{13}\frac{\sigma_r v^{n+1}_{r\ j,k+1/2}}{r_{j+1/2}} + c^E_{13}\frac{\delta_z v^{n+1}_{z\ j+1/2,k}}{\Delta z} + c^E_{33}\frac{\delta_r v^{n+1}_{r\ j,k+1/2}}{\Delta r}, \tag{76}$$

$$\frac{\delta_t \tau^{n+1/2}_{rz\ j,k}}{\Delta t} = \tilde{c}^E_{44}\left(\frac{\delta_r v^n_{z\ j-1/2,k}}{\Delta r} + \frac{\delta_z v^n_{r\ j,k-1/2}}{\Delta z}\right). \tag{77}$$

where $\tilde{c}^E_{44}$ is the harmonic average of the c^E_{44} coefficients surrounding the point (j,k). In a fluid medium $c^E_{44} = 0$, whereas in an isotropic elastic medium $c^E_{44} = \mu$.

Eqs. (67)–(72) fail to produce finite-difference approximations for the velocities and stresses at $r = r_{max}$ and $z = 0, z_{max}$ (the edges of the grid). The absorbing boundary conditions presented in Appendices A and B are used for this purpose. Lindman's absorbing boundary condition is used at the outer radial boundary when the elastic properties do not vary along that boundary. Otherwise, the multi-transmitting boundary conditions are used for extrapolating the stresses and velocities. Due to the nature of the problems studied here, the multi-transmitting formulas are also used along the upper and lower edges of the computational grid. In some problems, it is convenient to apply a symmetry boundary condition at the lower edge of the grid, in order to save computations and storage. In this case the shear stress as well as the velocity component normal to the boundary must vanish. This same boundary condition is applied along the axis $r = 0$.

Piezoelectricity

The first step in implementing the piezoelectric model is to update the stresses as if there were no piezoelectric effects. Denoting these updated quantities by $\bar{\tau}_{rr}^{n+3/2}$, $\bar{\tau}_{zz}^{n+3/2}$, $\bar{\tau}_{\theta\theta}^{n+3/2}$, and $\bar{\tau}_{rz}^{n+3/2}$, the following can be introduced

$$\Delta\tau_{\theta\theta}^{n+1} = \bar{\tau}_{\theta\theta}^{n+3/2} - \tau_{\theta\theta}^{n+1/2}, \tag{78}$$

$$\Delta\tau_{zz}^{n+1} = \bar{\tau}_{zz}^{n+3/2} - \tau_{zz}^{n+1/2}, \tag{79}$$

$$\Delta\tau_{rr}^{n+1} = \bar{\tau}_{rr}^{n+3/2} - \tau_{rr}^{n+1/2}, \tag{80}$$

$$\Delta\tau_{rz}^{n+1} = \bar{\tau}_{rz}^{n+3/2} - \tau_{rz}^{n+1/2}, \tag{81}$$

where the spatial indices were omitted for simplicity. These quantities are used in the source term of the discretized version of Eq. (45) which is shown next

$$\begin{aligned}
&\epsilon_{11}^{\varepsilon}\frac{\delta_{zz}\dot{\varphi}_{j,k-1/2}}{\Delta z^2} + \frac{\epsilon_{33}^{\varepsilon}}{r_j}\left(r_{j+1/2}\frac{\delta_r\dot{\varphi}_{j,k+1/2}}{\Delta r} - r_{j-1/2}\frac{\delta_r\dot{\varphi}_{j-1,k+1/2}}{\Delta r}\right)\\
&= \frac{d_{31}}{\Delta r}\delta_r\left[r_{j-1/2}\left(\Delta\tau_{\theta\theta\ j-1/2,k+1/2} + \Delta\tau_{zz\ j-1/2,k+1/2}\right)\right]\\
&+\frac{d_{33}}{\Delta r}\delta_r\left(r_{j-1/2}\Delta\tau_{rr\ j-1/2,k+1/2}\right) + \frac{d_{15}}{\Delta z}\delta_z\Delta\tau_{rz\ j,k}.
\end{aligned} \tag{82}$$

Eq. (82) forms a penta-diagonal system of linear equations which need to be solved for each time step. Notice that the time step index has been omitted in all the variables, since they are all at the same time step. This system is solved directly by Gaussian elimination (Golub and Van Loan, 1989). The stresses are finally corrected by using the following

$$\tau_{\theta\theta\ j+1/2,k+1/2}^{n+3/2} = \tau_{\theta\theta\ j+1/2,k+1/2}^{n+1/2} + \Delta\tau_{\theta\theta\ j+1/2,k+1/2}^{n+1} - \Delta t\ e_{31}\frac{\delta_r\dot{\varphi}_{j+1,k+1/2}^{n+3/2}}{\Delta r}, \tag{83}$$

$$\tau_{zz\ j+1/2,k+1/2}^{n+3/2} = \tau_{zz\ j+1/2,k+1/2}^{n+1/2} + \Delta\tau_{zz\ j+1/2,k+1/2}^{n+1} - \Delta t\ e_{31}\frac{\delta_r\dot{\varphi}_{j+1,k+1/2}^{n+3/2}}{\Delta r}, \tag{84}$$

$$\tau_{rr\ j+1/2,k+1/2}^{n+3/2} = \tau_{rr\ j+1/2,k+1/2}^{n+1/2} + \Delta\tau_{rr\ j+1/2,k+1/2}^{n+1} - \Delta t\ e_{33}\frac{\delta_r\dot{\varphi}_{j+1,k+1/2}^{n+3/2}}{\Delta r}, \tag{85}$$

$$\tau_{rz\ j,k}^{n+3/2} = \tau_{rz\ j,k}^{n+1/2} + \Delta\tau_{rz\ j,k}^{n+1} - \Delta t\ e_{15}\frac{\delta_z\dot{\varphi}_{j,k-1/2}^{n+3/2}}{\Delta z}. \tag{86}$$

Figure 3 shows the placement of the various elastic, piezoelectric, and electric quantities on the grid.

Constant Q Attenuation Model

As in the piezoelectric case, the quantities defined in (78)-(81) are used to update the ζ functions. If a frequency independent Q model for all viscoeleastic parameters is assumed, the analogues of Eq. (61) can be written as

$$\frac{d}{dt}\zeta_{\theta\theta l}(t) + \omega_l\zeta_{\theta\theta l}(t) = \gamma a_l\omega_l\frac{\Delta\tau_{\theta\theta}^{n+1}}{\Delta t}, \tag{87}$$

$$\frac{d}{dt}\zeta_{zzl}(t) + \omega_l\zeta_{zzl}(t) = \gamma a_l\omega_l\frac{\Delta\tau_{zz}^{n+1}}{\Delta t}, \tag{88}$$

$$\frac{d}{dt}\zeta_{rrl}(t) + \omega_l\zeta_{rrl}(t) = \gamma a_l\omega_l\frac{\Delta\tau_{rr}^{n+1}}{\Delta t}, \tag{89}$$

$$\frac{d}{dt}\zeta_{rzl}(t) + \omega_l\zeta_{rzl}(t) = \gamma a_l\omega_l\frac{\Delta\tau_{rz}^{n+1}}{\Delta t}, \tag{90}$$

where γ is defined in Appendix C.

Discretization of these equations is accomplished through the use of the difference and averaging operators

$$\frac{\delta_t\zeta_{\theta\theta l}^{n+1/2}}{\Delta t} + \omega_l\sigma_t\zeta_{\theta\theta l}^{n+1/2} = \gamma a_l\omega_l\frac{\Delta\tau_{\theta\theta}^{n+1}}{\Delta t}, \tag{91}$$

$$c\delta_t\zeta_{zzl}^{n+1/2}\Delta t + \omega_l\sigma_t\zeta_{zzl}^{n+1/2} = \gamma a_l\omega_l\frac{\Delta\tau_{zz}^{n+1}}{\Delta t}, \tag{92}$$

$$\frac{\delta_t \zeta_{rrl}^{n+1/2}}{\Delta t} + \omega_l \sigma_t \zeta_{rrl}^{n+1/2} = \gamma a_l \omega_l \frac{\Delta \tau_{rr}^{n+1}}{\Delta t}, \tag{93}$$

$$\frac{\delta_t \zeta_{rzl}^{n+1/2}}{\Delta t} + \omega_l \sigma_t \zeta_{rzl}^{n+1/2} = \gamma a_l \omega_l \frac{\Delta \tau_{rz}^{n+1}}{\Delta t}. \tag{94}$$

Once the ζ values are updated, the stresses can be corrected by

$$\tau_{\theta\theta}^{n+3/2} = \bar{\tau}_{\theta\theta}^{n+3/2} - \Delta t \sum_{l=1}^{L} \zeta_{\theta\theta l}^{n+3/2}, \tag{95}$$

$$\tau_{zz}^{n+3/2} = \bar{\tau}_{zz}^{n+3/2} - \Delta t \sum_{l=1}^{L} \zeta_{zzl}^{n+3/2}, \tag{96}$$

$$\tau_{rr}^{n+3/2} = \bar{\tau}_{rr}^{n+3/2} - \Delta t \sum_{l=1}^{L} \zeta_{rrl}^{n+3/2}, \tag{97}$$

$$\tau_{rz}^{n+3/2} = \bar{\tau}_{rz}^{n+3/2} - \Delta t \sum_{l=1}^{L} \zeta_{rzl}^{n+3/2}. \tag{98}$$

EXPERIMENTAL AND THEORETICAL RESULTS

Validation of the Elastic Borehole Model

In order to verify the theoretical and numerical models developed in this work, a series of experimental and theoretical comparisons will be described in this section. The first case considers only elastic wave propagation in an isotropic medium consisting of a fluid-filled borehole with a homogeneous formation. Figure 4 shows the source and receiver configuration, as well as the elastic parameters for the fluid and solid. The finite-difference and RAI waveforms for this model are shown in Figure 5, where the compressional, shear and Stoneley wave arrivals are clearly seen. The pressure point source in the finite-difference computation was implemented by feeding the normal stresses $(\tau_{rr}, \tau_{\theta\theta}, \tau_{zz})$. The source pulse shape is the second derivative of the Blackman-Harris window (Harris, 1978) centered at 10 kHz. This particular implementation requires that the pulse be first integrated before feeding it to the stresses. In Figure 6, the first and last waveforms of Figure 5 are shown individually to reveal the early arrivals. Notice the excellent match between the analytical and numerical waveforms, and in particular the absence of artificial edge reflections. This shows the excellent performance of the absorbing boundary conditions used in the finite-difference modeling. The minor differences are due to plotting interpolation, numerical dispersion, and to errors in the RAI computations.

Modeling of Piezoelectric Cylinders in a Borehole

To validate the transducer modeling, a series of simulations were conducted and compared with experimental data for a free-flooded piezoelectric cylinder (PZT-5). The inner and outer radial surfaces of the cylinder were electroplated and connected to an impedance analyser. The cylinder was then placed in an oil tank and impedance measurements were taken for a range of frequencies. A schematic diagram of the setup is shown in Figure 7. Table 2 shows the values of the elastic, piezoelectric, and dielectric constants for the particular PZT-5 material used in this work. The inner radius, outer radius and height of the transducer are respectively 0.00555 m, 0.00635 m, and 0.00635 m. Due to the inherent symmetry in this problem, only one quadrant was simulated. A 400×400 grid was used for this problem with $\Delta r = \Delta z = 4.0 \times 10^{-4}$ m. The number of time steps was 12000 with $\Delta t = 3.75 \times 10^{-8}$ s. The voltage pulse (second derivative of the Blackman-Harris window) and the resulting current flowing through the cylinder are shown in Figure 8. Notice the decaying resonance of the transducer in the current waveform due to internal losses and radiation into the fluid medium. In Figure 9, the magnitude and phase of the complex admittance are shown for the theoretical and experimental data. The input voltage and computed current waveforms were Fourier transformed to obtain the complex admittance. Obviously, this was not necessary for the experimental data since it was collected directly in the frequency domain. The small mismatches between the finite-difference and experimental results are mostly due to errors in the material constants, but overall the agreement is very good. Computations were also carried out using a hybrid method (Rogers, 1986), and the resulting magnitude and phase of the complex admittance are shown in Figure 10. Notice the poorer performance of this second method as compared to the finite-difference. Also since the hybrid method uses a radiation code to handle the propagation in the fluid, it would not be possible to model the transducer inside a fluid-filled borehole, which is the ultimate goal in this work.

Refering again to Figure 9, the peaks at 29.3 kHz, 61.8 kHz, 91.1 kHz, and 118.8 kHz correspond to resonances of the cylinder and the fluid in the cavity. To illustrate the vibration characteristics of the cylinder at these frequencies, the particle velocity waveforms (v_r, v_z) of the mid-surface of the cylinder were Fourier transformed, and the amplitude and phase at each resonance frequency were used to generate the mode shapes shown in Figure 11, and the particle paths shown in Figure 12. From these plots, one identifies the resonance at 29.3 kHz with the barrel mode, the resonances at 61.8 kHz and 91.1 kHz with the first and second order radial modes respectively, and the last resonance at 118.8 kHz with the length mode.

The radiation characteristics are best seen by computing the transmitter voltage response (TVR), which is defined as the ratio of the pressure in the fluid (normalized to a distance of 1 m from the geometrical center of the transducer) to the driving voltage for a given frequency. The TVR experimental data was collected by placing a small hydrophone at a distance of 0.114 m from the center of the transducer as shown in Figure 7 (broadside). The theoretical data was computed using the same geometry, with the addition of the axial pressure response (endfire). These results are shown in Figure 13. Notice the different frequency responses between the broadside and endfire configurations. In Figure 14 the radiation patterns corresponding to the four resonance frequencies described above are shown. These patterns were obtained by computing the pressure response at 21 positions equispaced along a quarter-circle surrounding the transducer. Its clear from these plots that the far-field radiation pattern is far from being that of a center of dilatation.

The fluid loading effects on the cylinder are best illustrated if one compares the admittances in both the fluid and air. The experimental data for the cylinder in air are shown in Figure 15. To study the loading from borehole reflections, a finite-difference computation was carried out with the PZT-5 cylinder in a fluid-filled borehole surrounded by an elastic formation with the following parameters; $\rho = 2500$ kg/m^3, $c = 5000$ m/s, and $s = 3000$ m/s. The borehole radius was taken to be four times the outer radius of the cylinder, in order to have the same ratio of radii as in the well logging situation. The theoretical results for the free field and borehole cases are shown in Figure 16. There are small differences between the two cases, as for instance the phase shift near 140 kHz, but they are too small to make the admittance a useful formation evaluation measurement.

To modify the frequency response of the transducer, a pair of circular steel plates were glued to the edges of the cylinder leaving air inside. The theoretical and experimental results for the transducer admittance in free field are shown in Figure 17. The discrepancies are mostly due to the boundary condition between the cylinder and the steel caps, which was assumed to be a welded contact in the theoretical simulation, but in reality is not. The TVR curves for this modified transducer are shown in Figure 18.

Finally, a theoretical computation was carried out for a scaled up version of the transducer used in the experiments, inside a fluid-filled borehole with the same fluid and formation properties as the ones shown in Figure 4. The inner radius, outer radius and height of the transducer are respectively 0.052 m, 0.06 m, and 0.152 m. The firing voltage and the current flowing through the free-flooded PZT-5 cylinder are shown in Figure 19. The center frequency of the voltage pulse was chosen such that it would coincide with the length mode of the transducer in order to obtain maximum output at that frequency. The magnitude and phase of the complex electrical admittance are presented in Figure 20. The length mode of the transducer is at 10 kHz. The pressure waveforms for both, point source excitation and transducer, are shown in Figure 21. The ringing character of the waveforms corresponding to the transducer case is due to the narrow band response at the length mode resonance. A semblance analysis (Kimball, 1984) of the two sets of waveforms was done, and the compressional, shear and Stoneley wave velocities in the case of a point source were found to be 3945 m/s, 2280 m/s, and 1424 m/s respectively. In the transducer case, coherence peaks were found for the compressional and shear waves, with velocities equal to 3907 m/s, and 2241 m/s respectively, but no Stoneley wave was detected due to the poor excitation of low frequencies by the transducer.

CONCLUSIONS

A new finite-difference time-domain modeling scheme has been developed to study the excitation, propagation, and detection of acoustic waves in complex borehole environments. A fully coupled elasto-electromagnetic model for a piezoelectric medium has been implemented, as well as a time-domain constant Q model, which has been generalized to model losses in a transversely isotropic piezoelectric medium.

The effectiveness and accuracy of the modeling scheme has been demonstrated through comparisons with analytical results and experimental data. Predictions of the model in the case of a piezoelectric cylinder source show that the transducer admittance is not very sensitive to formation parameters. Radiation patterns at various resonance frequencies show quite a deviation from the ideal center of dilatation. This fact is extremely important when interpreting data for near wellbore imaging or cross-well tomographic data. The effects of different transducer configurations, in order to modify frequency response or radiation pattern characteristics, can be quantitatively studied with the model developed in this paper. This is a very important feature when considering single well imaging applications of sonic logs or in evaluating radiation characteristics from downhole sources for cross-well tomography.

Also, the effects of bed boundaries, thin layers, borehole irregularities, and more general kinds of inhomogeneities in the elastic properties of the formation can be accurately studied with this scheme.

ACKNOWLEDGEMENTS

The author would like to thank Dr. H. Kunkel for many useful discussions concerning piezoelectric transducer behaviour and Dr. C.J. Randall for his extensive contributions to this work. Also, he would like to acknowledge support from Schlumberger-Doll Research during his leave at M.I.T.

REFERENCES

Auld, B.A., *Acoustic Fields and Waves in Solids*, Robert E. Krieger Publishing Company, 1990.

Ben-Menahem, A., and S. Kostek, The equivalent force-system of an explosion in a fluid-filled borehole, *M.I.T. Full Waveform Acoustic Logging Consortium Annual Report*, this issue, 1991.

Biot, M.A., Propagation of elastic waves in a cylindrical bore containing a fluid, *J. Appl. Phys., 23*, 997–1005, 1952.

Chan, A.K., and L. Tsang, Propagation of acoustic waves in a fluid-filled borehole surrounded by a concentrically layered transversely isotropic formation, *J. Acoust. Soc. Am., 74*, 1605–1616, 1983.

Cheng, C.H., and M.N. Toksöz, Elastic wave propagation in a fluid-filled borehole and synthetic acoustic logs, *Geophysics, 46*, 1042–1043, 1981.

Chew, W.C., S. Barone, B. Anderson, and C. Hennessy, Diffraction of axisymmetric waves in a borehole by bed boundary discontinuities, *Geophysics, 49*, 1586–1595, 1984.

Chiou, C.C., Electroacoustics of a piezoelectric cylindrical transducer in a fluid-filled borehole, Ph.D. Thesis, Georgia Institute of Technology, 1989.

Clayton, R., and B. Engquist, Absorbing boundary conditions for acoustic and elastic wave equations, *Bull. Seis. Soc. Am., 67*, 1529–1540, 1977.

Day, S.M., and J.B. Minster, Numerical simulation of attenuated wavefields using a Padé approximant method, *Geophys. J. Roy. Astr. Soc., 78*, 105–118, 1984.

Drumheller, D.S., and A. Kalnins, Dynamic shell theory for ferroelectric ceramics, *J. Acoust. Soc. Am., 47*, 1343–1353, 1969.

Emmerich, H., and M. Korn, Incorporation of attenuation into time-domain computations of seismic wave fields, *Geophysics, 52*, 1253–1264, 1987.

Engquist, B., and A. Majda, Radiation boundary conditions for acoustic and elastic wave calculations, *Comm. Pure Appl. Math., 32*, 314–357, 1979.

Golub, G.H., and C.F. Van Loan, *Matrix Computations*, The Johns Hopkins University Press, 1989.

Harris, F.J., On the use of windows for harmonic analysis with the discrete Fourier transform, *Proc. IEEE, 66*, 51–83, 1978.

Haskins, J.F., and J.L. Walsh, Vibrations of ferroelectric cylindrical shells with transverse isotropy. I. Radially polarized case, *J. Acoust. Soc. Am., 29*, 729–734, 1957.

Hunt, J.T., M.R. Knittel, and D. Barach, Finite element approach to acoustic radiation from elastic structures, *J. Acoust. Soc. Am., 55*, 269–280, 1974.

Kimball, C.V., and T.L. Marzetta, Semblance processing of borehole acoustic array data, *Geophysics, 49*, 274–281, 1984.

Kjartansson, E., Constant Q wave propagation and attenuation, *J. Geophys. Res., 84*, 4737–4748, 1979.

Kostek, S., and C.J. Randall, Borehole acoustic wave propagation in inhomogeneous and fractured formations: A finite-difference approach, submitted to *Geophysics*, 1990.

Liao, Z.P., H.L. Wong, B.P. Yang, and Y.F. Yuan, A transmitting boundary for transient wave analysis, *Scientia Sinica (series A), XXVII*, 1063–1076, 1984.

Lindman, E.L., Free-space boundary conditions for the time dependent wave equation, *J. Comp. Phys., 18*, 66–78, 1975.

Randall, C.J., Absorbing boundary conditions for the elastic wave equation, *Geophysics, 53*, 611–624, 1988.

Randall, C.J., Absorbing boundary conditions for the elastic wave equation: Velocity-stress formulation, *Geophysics, 54*, 1141–1152, 1989.

Rogers, P.H., SHIP (Simplified-Helmholtz-Integral Program): A fast computer program for calculating the acoustic radiation and radiation impedance for free-flooded-ring and finite-circular-cylinder sources, *Naval Research Laboratory Report 7240*, 1972.

Rogers, P.H., Mathematical model for a free-flooded piezoelectric cylinder transducer, *J. Acoust. Soc. Am., 80*, 13–18, 1986.

Rosenbaum, J.H., Synthetic microseismograms: Logging in porous formations, *Geophysics, 39*, 14–32, 1974.

Schenck, H.A., Improved integral formulation for acoustic radiation problems, *J. Acoust. Soc. Am., 44*, 41–58, 1967.

Schoenberg, M., T.L. Marzetta, J. Aron, and R.P. Porter, Space-time dependence of acoustic waves in a borehole, *J. Acoust. Soc. Am., 70*, 1496–1507, 1981.

Smith, R.R., J.T. Hunt, and D. Barach, Finite element analysis of acoustically radiating structures with applications to sonar transducers, *J. Acoust. Soc. Am., 54*, 1277–1288, 1973.

Stephen, R.A., F. Pardo-Casas, and C.H. Cheng, Finite-difference synthetic acoustic logs, *Geophysics, 50*, 1588–1609, 1985.

Tsang, L., Transient acoustic waves in a fluid-filled borehole with a horizontal bed boundary separating two solid formations, *J. Acoust. Soc. Am., 81*, 844–853, 1987.

Tsang, L., and D. Rader, Numerical evaluation of the transient acoustic waveform due to a point source in a fluid-filled borehole, *Geophysics, 44*, 1706–1720, 1979.

Tubman, K.M., C.H. Cheng, and M.N. Toksöz, Synthetic full waveform acoustic logs in cased boreholes, *Geophysics, 49*, 1051–1059, 1984.

Virieux, J., *P-SV* wave propagation in heterogeneous media: Velocity-stress finite difference method, *Geophysics, 51*, 889–901, 1986.

White, J.E., and R.E. Zechman, Response of an acoustic logging tool, *Geophysics, 33*, 302–310, 1968.

White, J.E., and C. Tongtaow, Cylindrical waves in transversely isotropic media, *J. Acoust. Soc. Am., 70*, 1147–1155, 1981.

Wilkinson, J.P.D., and M.J. DaCosta, Underwater behaviour of free-flooded ceramic ring transducers, *J. Eng. Ind., 93*, 819–825, 1971.

Zalesak, J.F., and P.H. Rogers, Low-frequency radiation characteristics of free-flooded ring transducers with application to a low-frequency directional hydrophone, *J. Acoust. Soc. Am., 56*, 1052–1058, 1974.

APPENDIX A

Absorbing Boundary Conditions: The Homogeneous Case

The absorbing boundary described here applies when the elastic properties along the edge of the computational grid are constant. The scheme is based on the original work of Lindman (1975), for the scalar wave equation. Randall (1988) generalized it to the elastic case formulated in terms of displacements, and later to the velocity-stress formulation (Randall, 1989). The cartesian scalar case will be briefly described, and then the generalized elastic case in terms of cylindrical coordinates.

Let a plane scalar wave $e^{i(\mathbf{k}\cdot\mathbf{r}-\omega t)}$ be incident upon an artificial boundary at $x = x_{max}$ in a homogeneous medium of velocity c. Then, along the $x-$axis the wave satisfies the equation

$$\frac{\partial\phi}{\partial t}+\frac{c}{\cos\theta}\frac{\partial\phi}{\partial x}=0. \tag{A.1}$$

Eq. (A.1) can be thought of as a relation between the time derivative and the normal derivative at the boundary, that allows waves to propagate to the right, off the grid. In general, there will be waves impinging at the grid boundaries with a range of incident angles θ. Lindman's idea is to use information at the boundaries to estimate $\cos\theta$ or $(\cos\theta)^{-1}$ locally for any incident wave and then use Eq. (A.1) to transport the wave across the boundary. Information available at the boundary is essentially ϕ, its tangential derivatives $\partial^n\phi/\partial z^n$, and its time derivatives $\partial^n\phi/\partial t^n$. Furthermore, it is desirable to keep the order of the time and tangential derivative low, so that the scheme is localized as much as possible.

For a harmonic plane wave $e^{i(\mathbf{k}\cdot\mathbf{r}-\omega t)}$, the following relation is readily established

$$\frac{1}{\cos\theta}=\left(1-\sin^2\theta\right)^{-1/2}=\left(1-\frac{c^2k_z^2}{\omega^2}\right)^{-1/2}. \tag{A.2}$$

Excluding evanescent waves, then $ck_z/\omega \leq 1$, and what is required is an approximation for $(1-u^2)^{-1/2}$, where $u = ck_z/\omega \leq 1$. Lindman proposed the following partial fraction expansion for this quantity

$$\frac{1}{\cos\theta}\approx 1+\sum_{m=1}^{M}\frac{\alpha_m(ck_z/\omega)^2}{1-\beta_m(ck_z/\omega)^2}, \tag{A.3}$$

where α_n and β_n are numerical coefficients. In particular, for $M = 3$, Lindman determined that the coefficients shown in Table A.1 provided an excellent fit to Eq. (A.2) for $0 \leq \theta \leq 89°$. This covers everything from normal incidence to near grazing incidence.

Substituting (A.3) into the frequency-wavenumber (k_z, ω) domain version of Eq. (A.1) gives

$$-i\omega\tilde{\phi} + c\frac{\partial\tilde{\phi}}{\partial x} = -\sum_{m=1}^{M}\tilde{h}_m, \tag{A.4}$$

where $\tilde{\phi}$ is the double Fourier transform of ϕ, and

$$\tilde{h}_m = \frac{\alpha_m c^2 k_z^2}{\omega^2 - \beta_m c^2 k_z^2}\left(c\frac{\partial\tilde{\phi}}{\partial x}\right). \tag{A.5}$$

Converting Eq. (A.5) to its time-space representation gives

$$\frac{\partial\phi}{\partial t} + c\frac{\partial\phi}{\partial x} = -\sum_{m=1}^{M} h_m, \tag{A.6}$$

where

$$\frac{\partial^2 h_m}{\partial t^2} - \beta_m c^2\frac{\partial^2 h_m}{\partial z^2} = \alpha_m c^2\frac{\partial^2}{\partial z^2}\left(c\frac{\partial\phi}{\partial x}\right). \tag{A.7}$$

Notice that in Eq. (A.6), the functions h_m on the right hand side act as a correction to the normal incidence absorbing boundary condition. Also, according to (A.7), these functions satisfy 1-D wave equations along the boundary with source terms given by $\alpha_m c^2\partial^2/\partial z^2(c\partial\phi/\partial x)$.

Generalization of Lindman's scalar absorbing boundary condition is possible if the medium is locally homogeneous along the boundary. For the P-SV problem at hand the velocity vector can be decomposed in terms of two scalar potentials ϕ and ψ, accounting for compressional and shear motion respectively

$$\mathbf{v} = \nabla\phi + \nabla\times(\psi\mathbf{e}_\theta). \tag{A.8}$$

These potentials satisfy scalar wave equations, which are

$$\frac{\partial^2\phi}{\partial t^2} = c^2\nabla\cdot\mathbf{v}, \tag{A.9}$$

$$\frac{\partial^2\psi\mathbf{e}_\theta}{\partial t^2} = -s^2\nabla\times\mathbf{v}. \tag{A.10}$$

The absorbing boundary conditions are thus expressed as

$$\frac{\partial\phi}{\partial t} + c\left(\frac{\partial\phi}{\partial r} + \frac{\phi}{r}\right) = -\sum_{m=1}^{M} h_m, \tag{A.11}$$

$$\frac{\partial\psi}{\partial t} + s\left(\frac{\partial\psi}{\partial r} + \frac{\psi}{r}\right) = -\sum_{m=1}^{M} g_m, \tag{A.12}$$

where the correction functions h_m and g_m satisfy the following 1-D wave equations along the outer radial boundary

$$\begin{aligned} \frac{\partial^2 h_m}{\partial t^2} - \beta_m c^2 \frac{\partial^2 h_m}{\partial z^2} &= \alpha_m c^2 \frac{\partial^2}{\partial z^2}\left(c\frac{\partial \phi}{\partial r}\right), && \text{(A.13)} \\ \frac{\partial^2 g_m}{\partial t^2} - \beta_m s^2 \frac{\partial^2 g_m}{\partial z^2} &= \alpha_m s^2 \frac{\partial^2}{\partial z^2}\left(s\frac{\partial \psi}{\partial r}\right). && \text{(A.14)} \end{aligned}$$

A stable finite-difference implementation of Eqs. (A.8)–(A.14) is presented next. In order to have all finite-difference approximations properly centered in space and time, the values of the potential along two layers of nodes next to the outer radial boundary are needed. The correction functions can be updated then by discretizing Eqs. (A.13) and (A.14),

$$\begin{aligned} \frac{\delta_{tt} h^{n-3/2}_{m,k+1/2}}{\Delta t^2} &= \beta_m c^2\, \frac{\delta_{zz} h^{n-1/2}_{m,k-1/2}}{\Delta z^2} + c^3 \frac{\delta_{zz}}{\Delta z^2}\sigma_t \left(\frac{\delta_r \phi^{n-1}_{J-1/2,k-1/2}}{\Delta r}\right), && \text{(A.15)} \\ \frac{\delta_{tt} g^{n-3/2}_{m,k}}{\Delta t^2} &= \beta_m s^2\, \frac{\delta_{zz} g^{n-1/2}_{m,k-1}}{\Delta z^2} + c^3 \frac{\delta_{zz}}{\Delta z^2}\sigma_t \left(\frac{\delta_r \psi^{n-1}_{J-1,k-1}}{\Delta r}\right). && \text{(A.16)} \end{aligned}$$

Equations (A.15) and (A.16) cannot be applied to compute $h_{m,1/2}$, $h_{m,K-1/2}$, $g_{m,0}$, and $g_{m,K}$. A 1-D multi-transmitting formula is used to generate these values (refer to Appendix B). The potentials at the interior layers are updated by discretizing equations (A.9) and (A.10)

$$\begin{aligned} \frac{\delta_{tt}\phi^{n-1}_{J-1/2,k+1/2}}{\Delta t^2} &= c^2 \frac{\delta_r v^n_{r\ J-1,k+1/2}}{\Delta r} + \frac{c^2}{J\Delta r}\sigma_r v^n_{r\ J-1,k+1/2} \\ &\quad + s^2 \frac{\delta_z v^n_{z\ J-1/2,k}}{\Delta z}, && \text{(A.17)} \\ \frac{\delta_{tt}\psi^{n-1}_{J-1,k}}{\Delta t^2} &= s^2 \frac{\delta_r v^n_{z\ J-1/2,k}}{\Delta r} - s^2 \frac{\delta_z v^n_{r\ J-1,k-1/2}}{\Delta z}, && \text{(A.18)} \end{aligned}$$

where the potentials $\phi_{J-1/2,K+1/2}$, $\psi_{J-1,K}$, and $\psi_{J-1,0}$ are computed by a 1-D multi-transmitting formula. Lindman's approximations (A.11) and (A.12), can now be used to transport the potentials across the boundary

$$\begin{aligned} \sigma_r \frac{\delta_t \phi^n_{J-1/2,k+1/2}}{\Delta t} + c\,\sigma_t \frac{\delta_r \phi^n_{J-1/2,k+1/2}}{\Delta r} + \frac{c}{J\Delta r}\sigma_t \left(\sigma_r \phi^n_{J-1/2,k+1/2}\right) & \\ = -\sum_{m=1}^{M} h^{n+1/2}_{m,k+1/2}, && \text{(A.19)} \end{aligned}$$

$$\sigma_r \frac{\delta_t \psi^n_{J-1,k}}{\Delta t} + s\ \sigma_t \frac{\delta_r \psi^n_{J-1,k}}{\Delta r} + \frac{s}{J\Delta r} \sigma_t \left(\sigma_r \psi^n_{J-1,k}\right)$$

$$= - \sum_{m=1}^{M} g^{n+1/2}_{m,k}, \qquad \text{(A.20)}$$

where the potentials at $\phi_{J+1/2,K+1/2}$, $\psi_{J+1,K}$, and $\psi_{J+1,0}$ are found through the application of the 1-D multi-transmitting formula. The velocity components can now be updated by discretizing equation (A.18)

$$v^{n+1}_{r\ J,k+1/2} = \frac{\delta_r \phi^{n+1}_{J-1/2,k+1/2}}{\Delta r} - \frac{\delta_z \psi^{n+1}_{J,k}}{\Delta z}, \qquad \text{(A.21)}$$

$$v^{n+1}_{z\ J-1/2,k} = \frac{\delta_r \psi^{n+1}_{J-1,k}}{\Delta r} + \frac{\sigma_t \psi^{n+1}_{J-1,k}}{r_{J-1/2}} + \frac{\delta_z \phi^{n+1}_{J-1/2,k-1/2}}{\Delta z}. \qquad \text{(A.22)}$$

APPENDIX B

Absorbing Boundary Conditions: The Heterogeneous Case

In this appendix we describe an absorbing boundary condition which can be used in cases where the elastic properties are inhomogeneous along the boundary, e.g., the top and bottom boundaries in acoustic well logging. We will derive the multi-transmitting formulas here in the case of scalar waves and in cartesian coordinates. We will modify them later to account for cylindrical symmetry.

A plane wave solution to the scalar wave equation in the time domain can be written as $u(ct - s\cos\theta)$, where the direction of the plane wave makes an angle θ with the x-axis. Moreover, an arbitrary wave can be approximated by a summation of plane waves with different angles. Therefore,

$$\phi(x,t) = \sum_i u_i(ct - x\cos\theta_i). \qquad \text{(B.1)}$$

But if $\phi(x,t)$ represents only a single plane wave, then $\phi(x, t+\Delta t) = \phi(x - c\Delta t/\cos\theta, t)$, which is a primitive absorbing boundary condition to update the boundary point at x with the interior point if the angle of the wave θ is known. We can write

$$\begin{aligned} \phi(x, t+\Delta t) &= \sum_i u_i \left(c(t+\Delta t) - x\cos\theta_i\right) \\ &= \sum_i u_i \left(ct - (x - \alpha c\Delta t)\cos\theta_i + c\Delta t(1 - \alpha\cos\theta_i)\right) \\ &= \sum_i u_i(\eta_i + \xi_i), \end{aligned} \qquad \text{(B.2)}$$

where

$$\begin{aligned}\eta_i &= ct - (x - \alpha c\Delta t)\cos\theta_i, && \text{(B.3)}\\ \xi_i &= c\Delta t(1 - \alpha\cos\theta_i). && \text{(B.4)}\end{aligned}$$

To make this equation useful we still have to express $u_i(\eta_i+\xi_i)$ in terms of $u_i(\eta_i+\nu\xi_i)$, where $\nu \geq 0$. If only one plane wave component exists, α can be chosen to equal $(\cos\theta)^{-1}$, rendering $\xi = 0$, and this problem disappears. But in general, a spectrum of plane waves exists for which an absorbing boundary condition is needed. Introducing the following difference operator

$$\Delta u(\eta+\xi) = u(\eta+\xi) - u(\eta), \tag{B.5}$$

then,

$$\Delta^m u(\eta+\xi) = \Delta^{m-1}u(\eta+\xi) - \Delta^{m-1}u(\eta), \tag{B.6}$$

for $m > 0$ and $\Delta^0 u(\eta) = 1$. Using this relationship, it can be shown that

$$u(\eta+\xi) = \sum_{m=1}^{N} \Delta^{m-1}u(\eta) + \Delta^N u(\eta+\xi). \tag{B.7}$$

The above equation is just the finite-difference analogue of the N^{th}-order Taylor series expansion. In the limit when $\xi \to 0$, we have

$$\Delta^N u(\eta+\xi) \sim \xi^N \frac{d^N}{d\eta^N}u(\eta). \tag{B.8}$$

Therefore for small ξ, the last term in (B.7) can be neglected. As a result,

$$u(\eta+\xi) \approx \sum_{m=1}^{N} \Delta^{m-1}u(\eta), \tag{B.9}$$

or

$$u(\eta+\xi) \approx \sum_{j=1}^{N}(-1)^{j+1}C_j^N u\left(\eta - (j-1)\xi\right), \tag{B.10}$$

where

$$C_j^N = \frac{N!}{j!(N-j)!}. \tag{B.11}$$

Using (B.10) in (B.2) together with the definitions of η_i and ξ_i we obtain

$$\phi(x, t+\Delta t) = \sum_{j=1}^{N}(-1)^{j+1}C_j^N \phi\left(x - j\alpha c\Delta t, t - (j-1)\Delta t\right). \tag{B.12}$$

Since α multiplies c in the above, we do not need to know the velocity c accurately to apply this boundary condition. We take advantage of this fact in the generalization of this scheme to elastic wave propagation in the sense that we apply it to all necessary field quantities (velocity or stress) at the particular boundary using an average of the local compressional and shear wave velocities. For all practical purposes, α can be chosen to be 1 in (B.12). When $\alpha = 1$, $\xi = 0$ in (B.4) for a normally incident wave. Moreover, ξ becomes larger for larger angles of incidence. Hence, the interpolation scheme in (B.12) is exact for a normally incident wave, and corrects for an obliquely incident wave.

To apply (B.12), an interpolation scheme is necessary since the interior points $x - j\alpha c\Delta t$ (for $\alpha = 1$) do not lie on the grid points. Using quadratic interpolation we can write

$$\phi(x - c\Delta t, t) = \frac{(2-s)(1-s)}{2}\phi_1^1(x) + s(2-s)\phi_2^1(x) + \frac{s(s-1)}{2}\phi_3^1(x), \tag{B.13}$$

where

$$\phi_i^m(x) = \phi\left(x - (i-1)\Delta x, t - (m-1)\Delta t\right), \tag{B.14}$$

and

$$s = c\Delta t/\Delta x. \tag{B.15}$$

Eq. (B.13) can be expressed as

$$\phi(x - c\Delta t, t) = \mathbf{T}^1 \cdot \mathbf{\Phi}_3^1(x), \tag{B.16}$$

where

$$\begin{aligned} \mathbf{T}^1 &= \left[\begin{array}{ccc} (2-s)(1-s)/2 & s(2-s) & s(s-1)/2 \end{array} \right], & \text{(B.17)} \\ \mathbf{\Phi}_3^1 &= \left[\begin{array}{ccc} \phi_1^1(x) & \phi_2^1(x) & \phi_3^1(x) \end{array} \right]^T. & \text{(B.18)} \end{aligned}$$

Similarly,

$$\begin{aligned} \phi(x - 2c\Delta t, t - \Delta t) &= \mathbf{T}^1 \cdot \left[\begin{array}{ccc} \phi_1^2(x - c\Delta t) & \phi_2^2(x - c\Delta t) & \phi_3^2(x - c\Delta t) \end{array} \right]^T \\ &= \mathbf{T}^1 \cdot \mathbf{\Phi}_3^2(x - c\Delta t). & \text{(B.19)} \end{aligned}$$

Since

$$\begin{aligned} \phi_1^2(x - c\Delta t) &= \mathbf{T}^1 \cdot \mathbf{\Phi}_3^2(x), & \text{(B.20)} \\ \phi_2^2(x - c\Delta t) &= \phi_1^2(x - \Delta x - c\Delta t) = \mathbf{T}^1 \cdot \mathbf{\Phi}_3^2(x - \Delta x), & \text{(B.21)} \\ \phi_3^2(x - c\Delta t) &= \phi_1^2(x - 2\Delta x - c\Delta t) = \mathbf{T}^1 \cdot \mathbf{\Phi}_3^2(x - 2\Delta x), & \text{(B.22)} \end{aligned}$$

where $\mathbf{\Phi}_3^2(x) = \left[\phi_1^2(x)\ \ \phi_2^2(x)\ \ \phi_3^2(x)\right]^T$, $\mathbf{\Phi}_3^2(x-\Delta x) = \left[\phi_2^2(x)\ \ \phi_3^2(x)\ \ \phi_4^2(x)\right]^T$, and $\mathbf{\Phi}_3^2(x-2\Delta x) = \left[\phi_3^2(x)\ \ \phi_4^2(x)\ \ \phi_5^2(x)\right]^T$, we can write Eqs. (B.20)–(B.22) as

$$\mathbf{\Phi}_3^2(x-c\Delta t) = \begin{bmatrix} \mathbf{T}^1 & 0 & 0 \\ 0 & \mathbf{T}^1 & 0 \\ 0 & 0 & \mathbf{T}^1 \end{bmatrix} \cdot \mathbf{\Phi}_5^2(x), \tag{B.23}$$

where

$$\mathbf{\Phi}_5^2(x) = \begin{bmatrix} \phi_1^2(x) & \phi_2^2(x) & \phi_3^2(x) & \phi_4^2(x) & \phi_5^2(x) \end{bmatrix}^T. \tag{B.24}$$

Consequently, from (B.19) and (B.23) one obtains

$$\phi(x-2c\Delta t, t-\Delta t) = \mathbf{T}^1 \cdot \begin{bmatrix} \mathbf{T}^1 & 0 & 0 \\ 0 & \mathbf{T}^1 & 0 \\ 0 & 0 & \mathbf{T}^1 \end{bmatrix} \cdot \mathbf{\Phi}_5^2(x) = \mathbf{T}^2 \cdot \mathbf{\Phi}_5^2(x). \tag{B.25}$$

After applying this idea recursively, one obtains

$$\phi(x-jc\Delta t, t-(j-1)\Delta t) = \mathbf{T}^j \cdot \phi_{2j+1}^j(x), \tag{B.26}$$

where

$$\mathbf{T}^j = \mathbf{T}^1 \cdot \begin{bmatrix} \mathbf{T}^{j-1} & 0 & 0 \\ 0 & \mathbf{T}^{j-1} & 0 \\ 0 & 0 & \mathbf{T}^{j-1} \end{bmatrix}, \tag{B.27}$$

is a row vector of length $2j+1$, and

$$\mathbf{\Phi}_{2j+1}^j(x) = \begin{bmatrix} \phi_1^j(x) & \phi_2^j(x) & \dots & \phi_{2j+1}^j(x) \end{bmatrix}^T. \tag{B.28}$$

The absorbing boundary condition (B.12) becomes

$$\phi(x, t+\Delta t) = \sum_{j=1}^{N} (-1)^{j+1} C_j^N \mathbf{T}^j \cdot \mathbf{\Phi}_{2j+1}^j(x). \tag{B.29}$$

It is relatively easy to establish a relation between this family of multi-transmitting boundary conditions and the well known Engquist-Majda boundary condition. When $N = 1$ the multi-transmitting formula is associated with the following equation

$$\frac{1}{c}\frac{\partial \phi}{\partial t} + \xi \frac{\partial \phi}{\partial x} = 0, \tag{B.30}$$

which for $\xi = 1$ is the first-order Engquist-Majda boundary condition (viscous boundary). A second order approximation can be obtained with $N = 2$ in (B.12), and it is associated with

$$\frac{1}{c^2}\frac{\partial^2 \phi}{\partial t^2} + \frac{2\xi}{1+\xi^2}\frac{\partial^2 \phi}{\partial x \partial t} - \frac{\xi^2}{1+\xi^2}\frac{\partial^2 \phi}{\partial x^2} = 0, \tag{B.31}$$

which for $\xi = 1$ is represented by the first-order Engquist-Majda boundary condition.

In our computations we use the multi-transmitting formula (B.12) for propagating the fields on the top and bottom boundaries of the computational domain. The field variables involved in this case are the axial component of the particle velocity v_z and the shear component of stress τ_{rz}. If elastic properties vary along the outer radial boundary we also use (B.12) to propagate the radial component of the particle velocity v_r and the shear component of stress τ_{rz}, but here we take the care to expand the cylindrical waves into plane waves using an amplitude factor derived from a WKBJ approximation. In all computations shown in this paper, a value of $N = 3$ was used.

APPENDIX C

Coefficients for the Constant Q Model

The Debye functions which approximate Q^{-1} are symmetric functions on a logarithmic scale and have a half-width of 1.144 decades. In order to have a Q^{-1} which is reasonably constant over a frequency band, the most natural choice of the relaxation frequencies ω_l is a logarithmic equidistant distribution over the frequency band of interest. The half-width of the Debye functions gives an upper limit for the ratio ω_l/ω_{l-1}. In our computations we use a ratio $\omega_l/\omega_{l-1} = 3$. To determine the weight factors a_l, the following procedure can be used for any frequency dependent Q law. Q of the generalized Maxwell solid (63) is required to be identical to a given $\tilde{Q}(\omega)$ law at certain discrete frequencies $\tilde{\omega}_p$. Defining

$$y_l = \frac{\delta M}{M_r} a_l, \qquad \text{(C.1)}$$

and substituting into Eq. (63) gives

$$\sum_{l=1}^{L} \frac{\tilde{\omega}_k \left[\omega_l - \tilde{Q}^{-1}(\tilde{\omega}_p)\tilde{\omega}_p\right]}{\omega^2 + \tilde{\omega}_p^2} y_l = \tilde{Q}^{-1}(\tilde{\omega}_p) \qquad p = 1, ..., P. \qquad \text{(C.2)}$$

This constitutes a linear system of equations for the unknowns y_l. A convenient choice for the $\tilde{\omega}_p$ is to use the relaxation frequencies ω_l and the frequencies in the middle between adjacent ω_l, i.e., $\tilde{\omega}_1 = \omega_1$, $\tilde{\omega}_{p+1} = \tilde{\omega}_p(\omega_2/\omega_1)^{1/2}$. Then $P = 2L - 1$ and the system (C.2) is overdetermined and can be solved by a least-squares algorithm. Denoting by $\mathbf{A}$ the matrix of coefficients in (C.2), $\mathbf{y}$ the column vector of unknowns and $\mathbf{z}$ the column vector composed of the values in the right hand side of (C.2) we can write the least-squares solution as

$$\mathbf{y} = (\mathbf{A}^t\mathbf{A})^{-1}\mathbf{A}^t\mathbf{z}. \qquad \text{(C.3)}$$

From (C.1) and the normalization condition for a_l we have

$$a_l = y_l \left(\sum_{l=1}^{L} y_l \right)^{-1} . \tag{C.4}$$

The equation for the $\zeta_l(t)$ functions can then be written as

$$\frac{d}{dt}\zeta_l(t) + \omega_l \zeta_l(t) = \gamma a_l \omega l \varepsilon(t), \tag{C.5}$$

where

$$\gamma = \left(\sum_{l=1}^{L} y_l \right) \left(1 + \sum_{l=1}^{L} y_l \right)^{-1} . \tag{C.6}$$

	ε						$\mathbf{E}$		
τ	c_{11}^{E}	c_{12}^{E}	c_{13}^{E}	0	0	0	0	0	$-e_{31}$
	c_{12}^{E}	c_{11}^{E}	c_{13}^{E}	0	0	0	0	0	$-e_{31}$
	c_{13}^{E}	c_{13}^{E}	c_{33}^{E}	0	0	0	0	0	$-e_{33}$
	0	0	0	c_{44}^{E}	0	0	0	$-e_{15}$	0
	0	0	0	0	c_{44}^{E}	0	$-e_{15}$	0	0
	0	0	0	0	0	c_{66}^{E}	0	0	0
$\mathbf{D}$	0	0	0	0	e_{15}	0	ϵ_{11}^{S}	0	0
	0	0	0	e_{15}	0	0	0	ϵ_{11}^{S}	0
	e_{31}	e_{31}	e_{33}	0	0	0	0	0	ϵ_{33}^{S}

Table 1. Elastic, piezoelectric, and dielectric coefficients relating the mechanical and electrical field variables.

ρ	7.750×10^{3} kg/m^{3}
c^{E}_{11}	9.767×10^{10} Pa
c^{E}_{12}	5.235×10^{10} Pa
c^{E}_{13}	5.235×10^{10} Pa
c^{E}_{33}	9.767×10^{10} Pa
c^{E}_{44}	2.266×10^{10} Pa
e_{31}	-6.075 C/m^{2}
e_{33}	18.625 C/m^{2}
e_{15}	14.145 C/m^{2}
ϵ^{ϵ}_{11}	5.440×10^{-9} F/m
ϵ^{ϵ}_{33}	6.000×10^{-9} F/m
Q	75

Table 2. Material constants for PZT-5.

	$m = 1$	$m = 2$	$m = 3$
α_m	0.3264	0.1272	0.0309
β_m	0.7375	0.98384	0.9996472

Table A.1. Coefficients for the rational expansion approximation of the inverse square root operator used in Lindman's absorbing boundary condition.

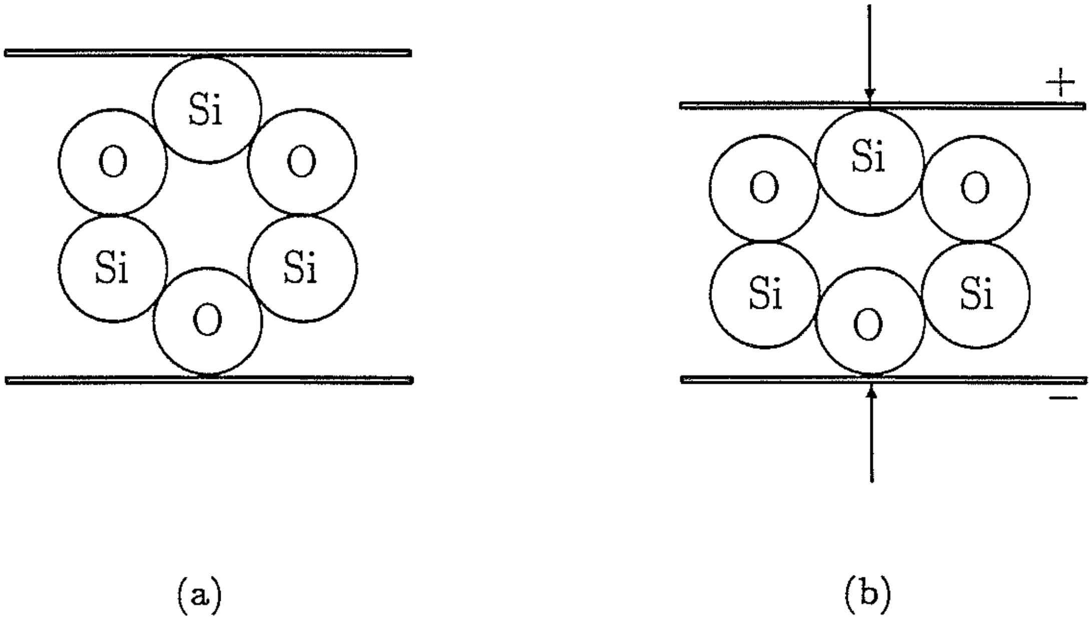

(a) (b)

Figure 1: Direct piezoelectric effect.

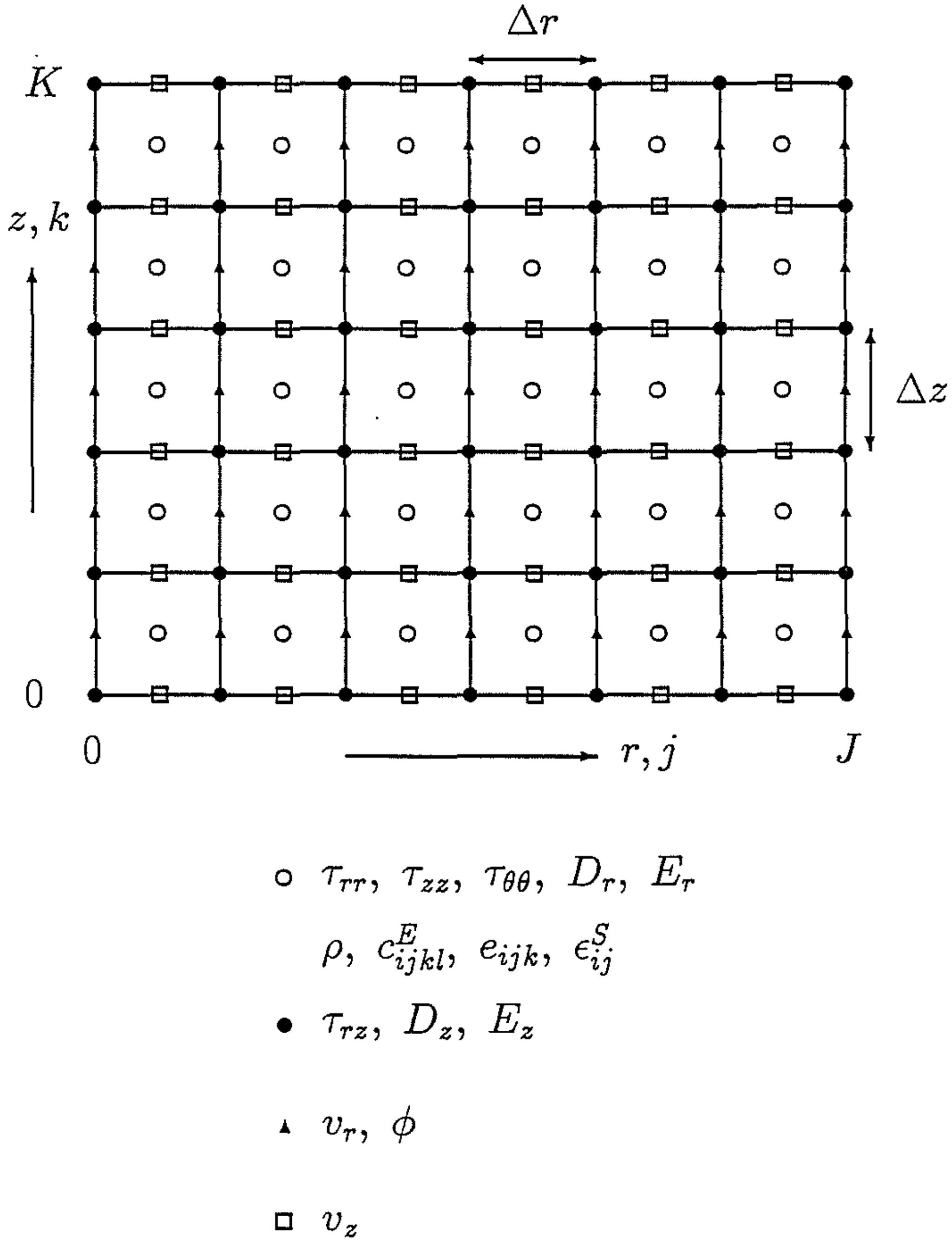

Figure 2: Staggered finite-difference grid showing the placement of the field variables and elastic parameters.

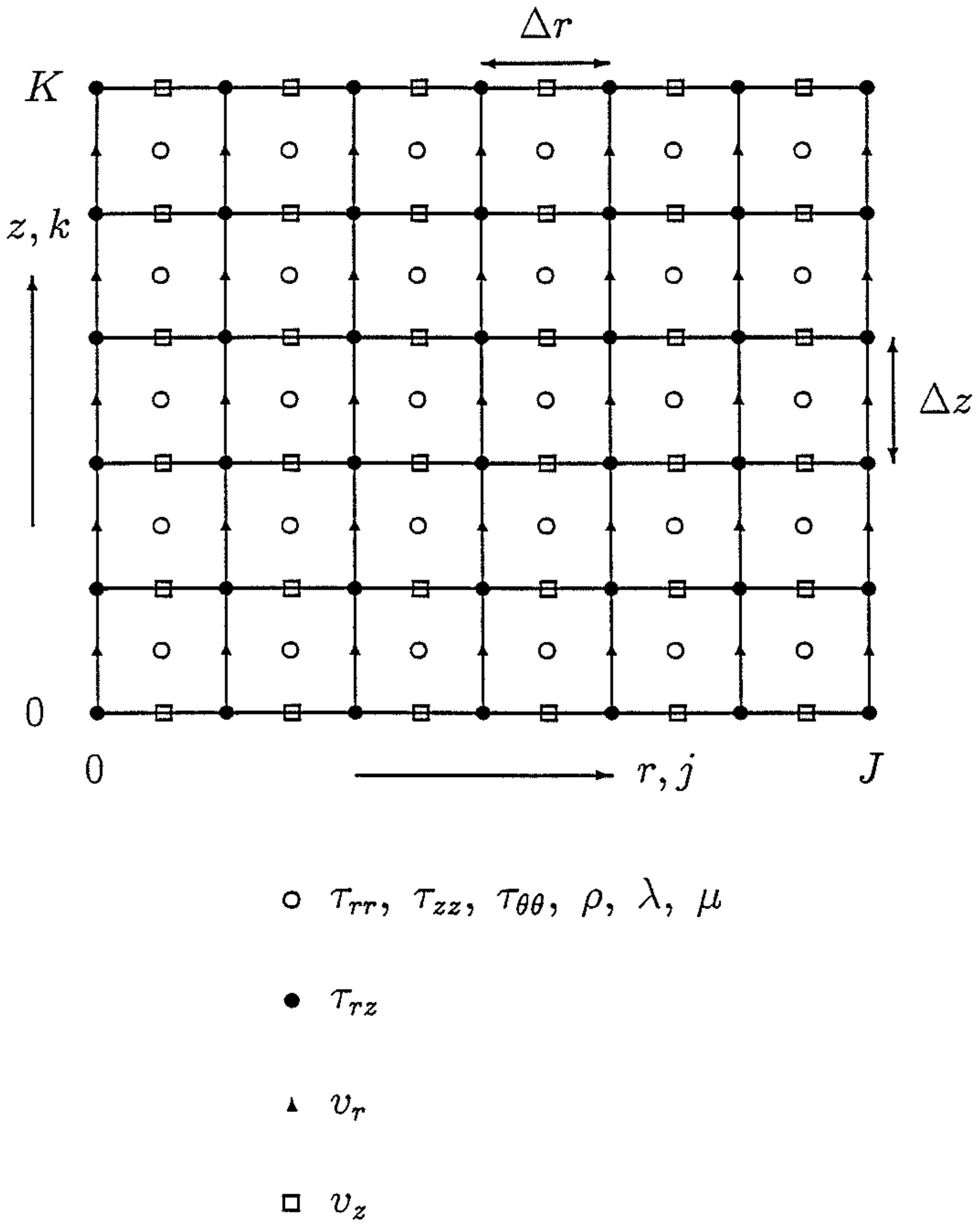

Figure 3: Staggered finite-difference grid showing the placement of the field variables and material parameters.

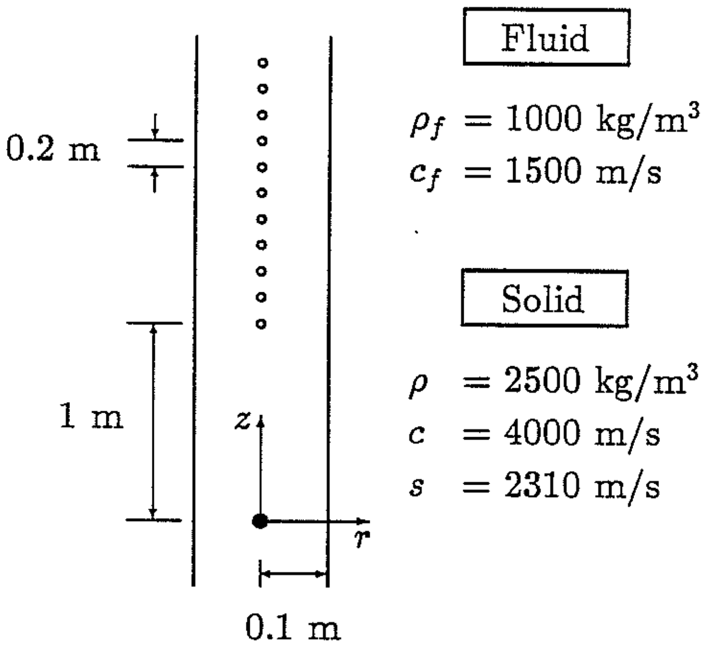

Figure 4: Geometry of fluid-filled borehole, source-receiver arrangement, and elastic properties.

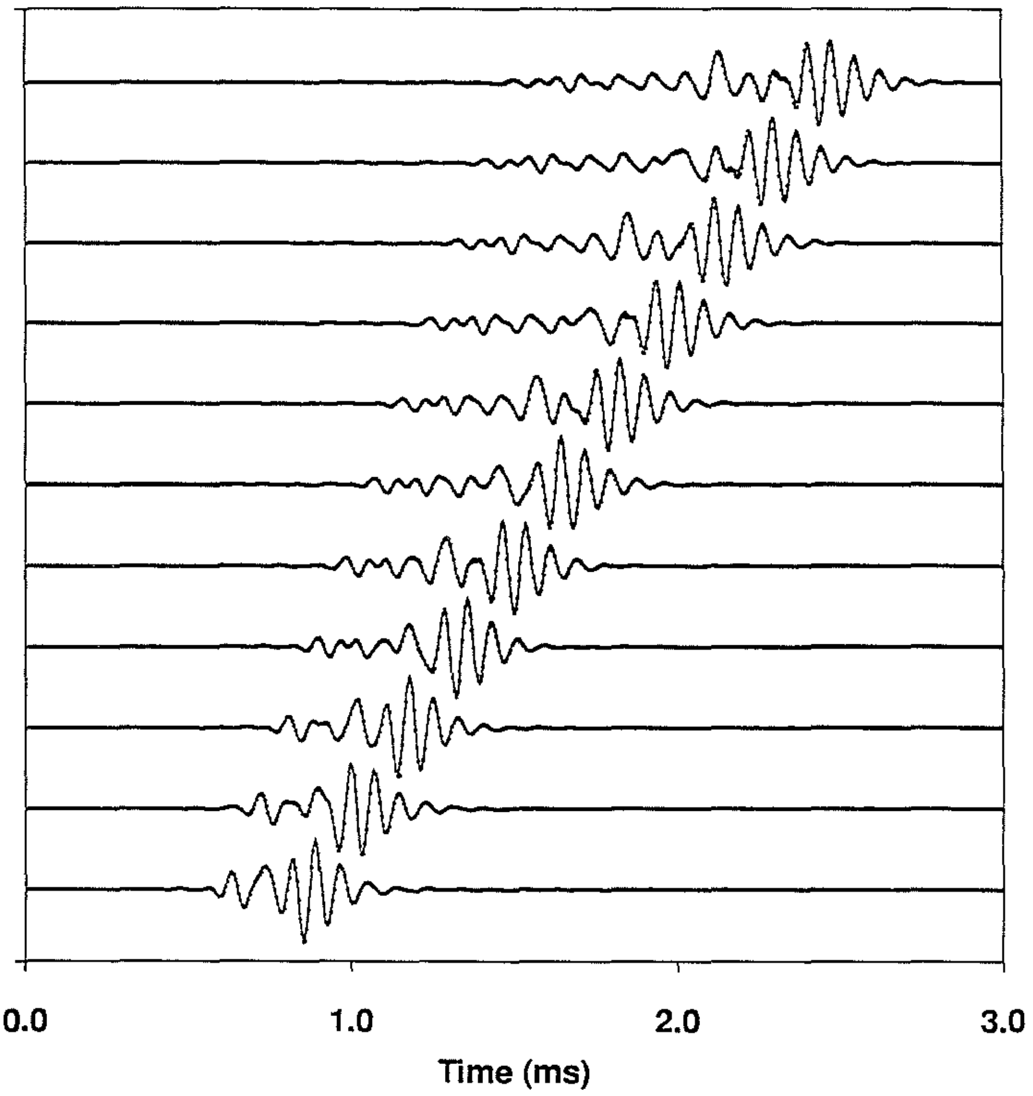

Figure 5: Finite-difference (solid) and RAI (dotted) waveforms for the case shown in Figure 4.

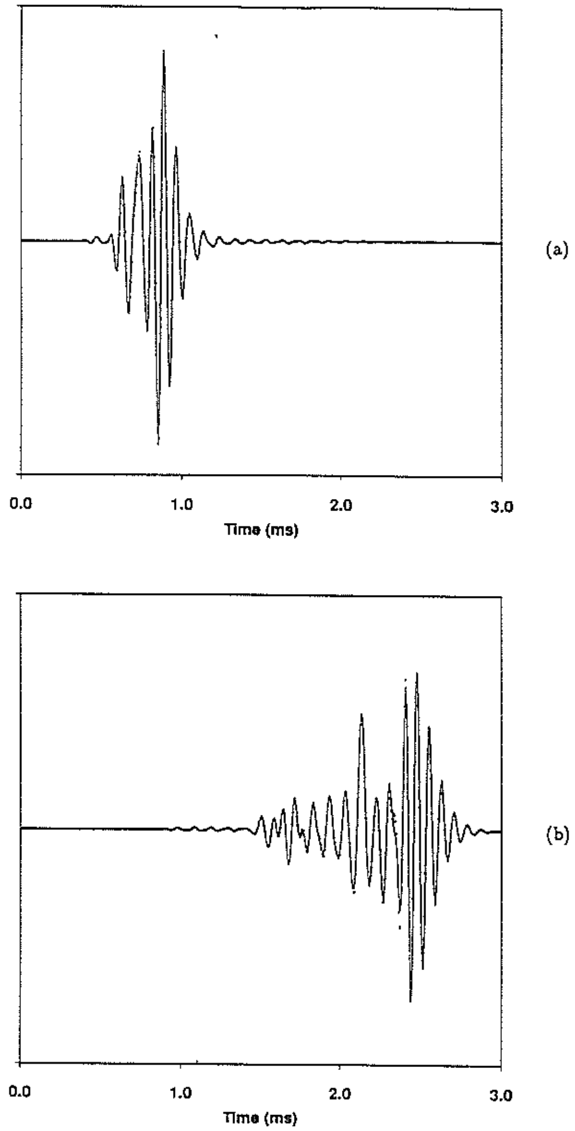

Figure 6: Finite-difference (solid) and RAI (dotted) waveforms. (a) Receiver #1. (b) Receiver #11.

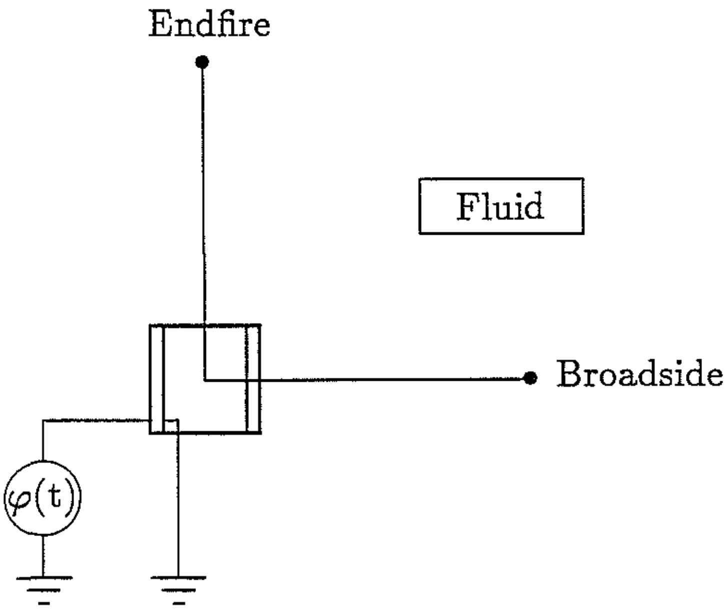

Figure 7: Experimental setup for admittance and TVR measurements. Distance between broadside (endfire) pressure point measurement and geometrical center of PZT-5 cylinder is 0.114 m.

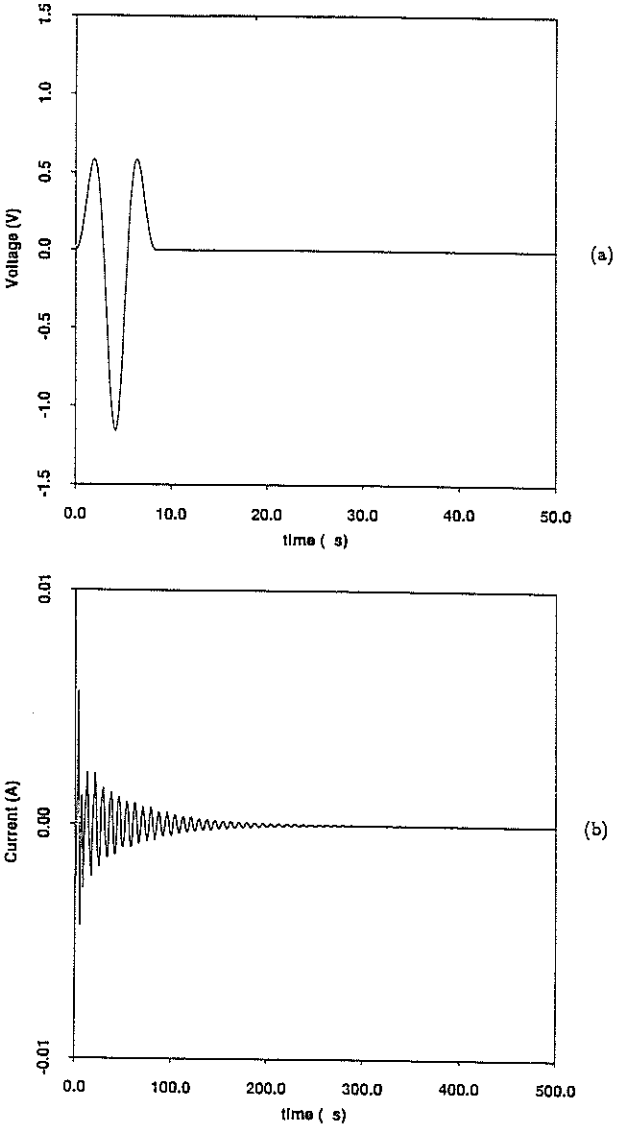

Figure 8: Input-output waveforms in finite-difference simulation of PZT-5 cylinder in oil. (a) Firing voltage. (b) Electric current.

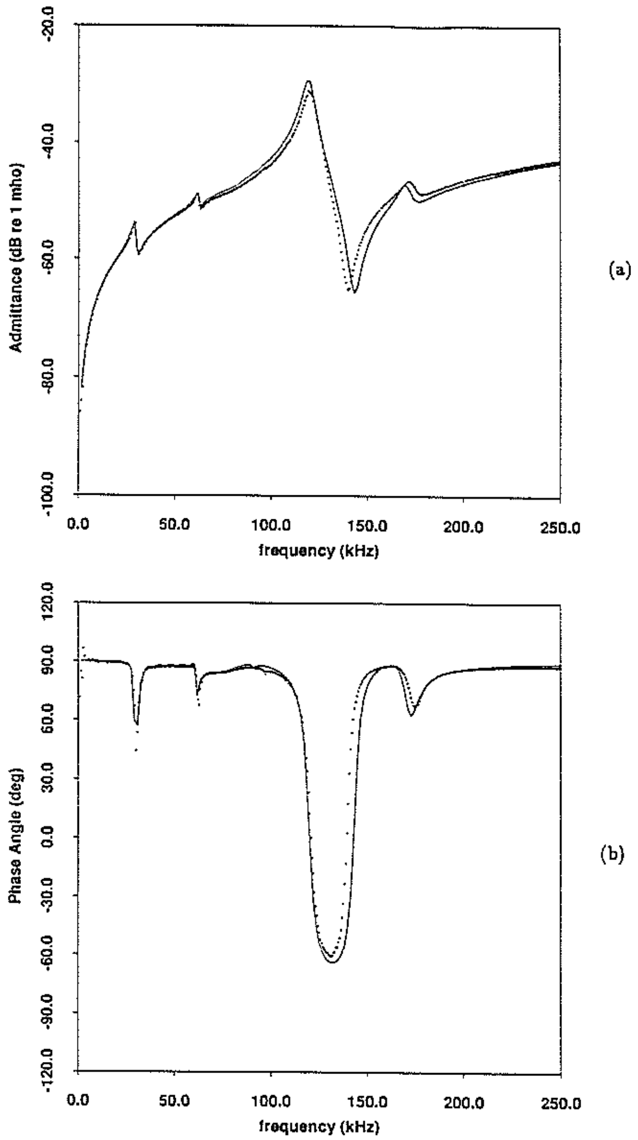

Figure 9: Finite-difference (solid) and experimental (dotted) admittance for PZT-5 cylinder in oil. (a) Magnitude. (b) Phase Angle.

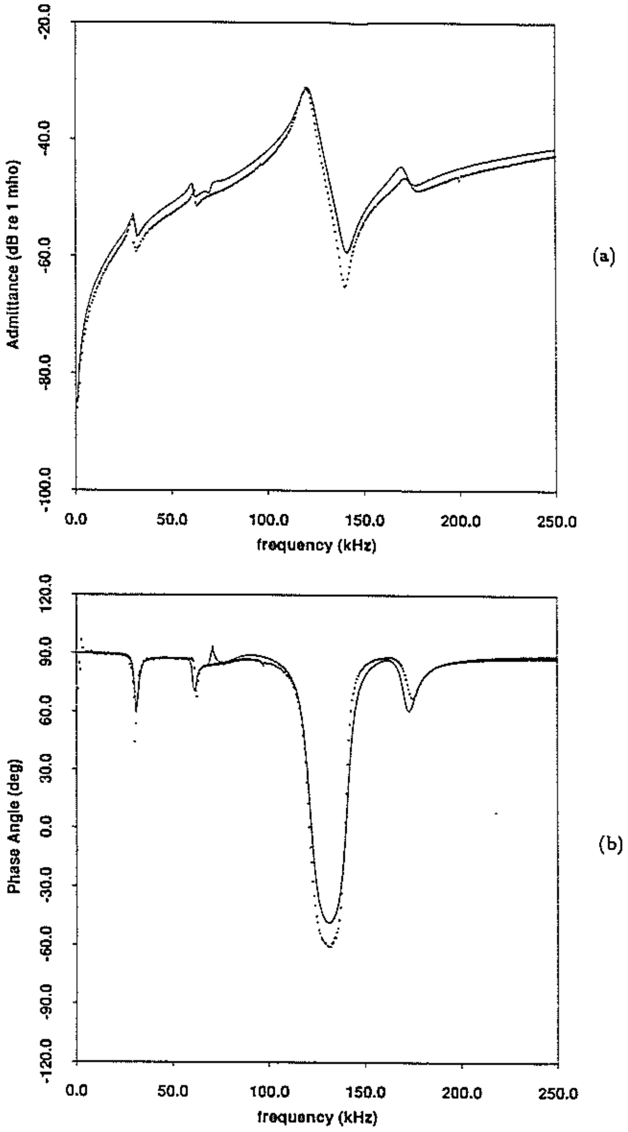

Figure 10: Semi-analytical (solid) and experimental (dotted) admittance for PZT-5 cylinder in oil. (a) Magnitude. (b) Phase Angle.

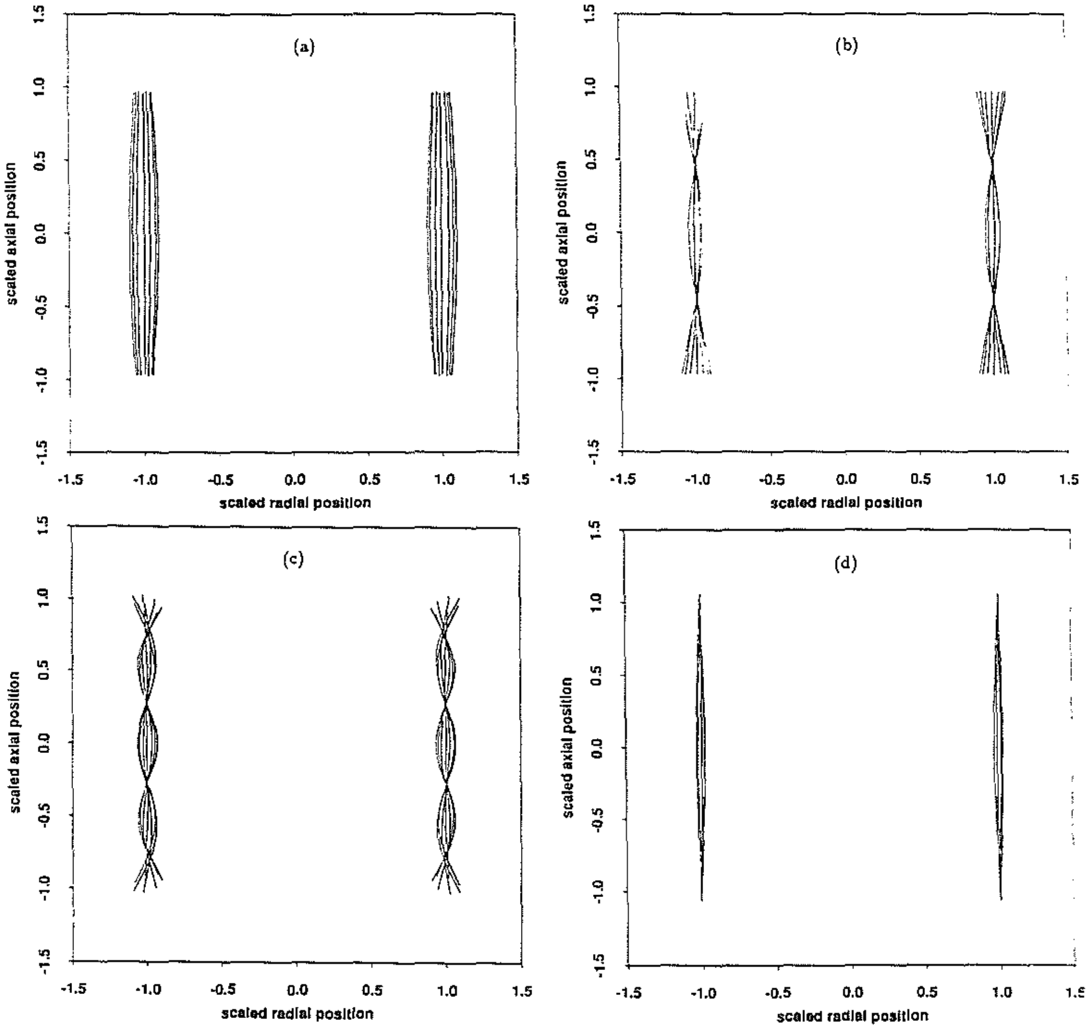

Figure 11: Mode shapes for PZT-5 cylinder in oil. (a) Barrel mode. (b) First radial mode. (c) Second radial mode. (d) Length mode.

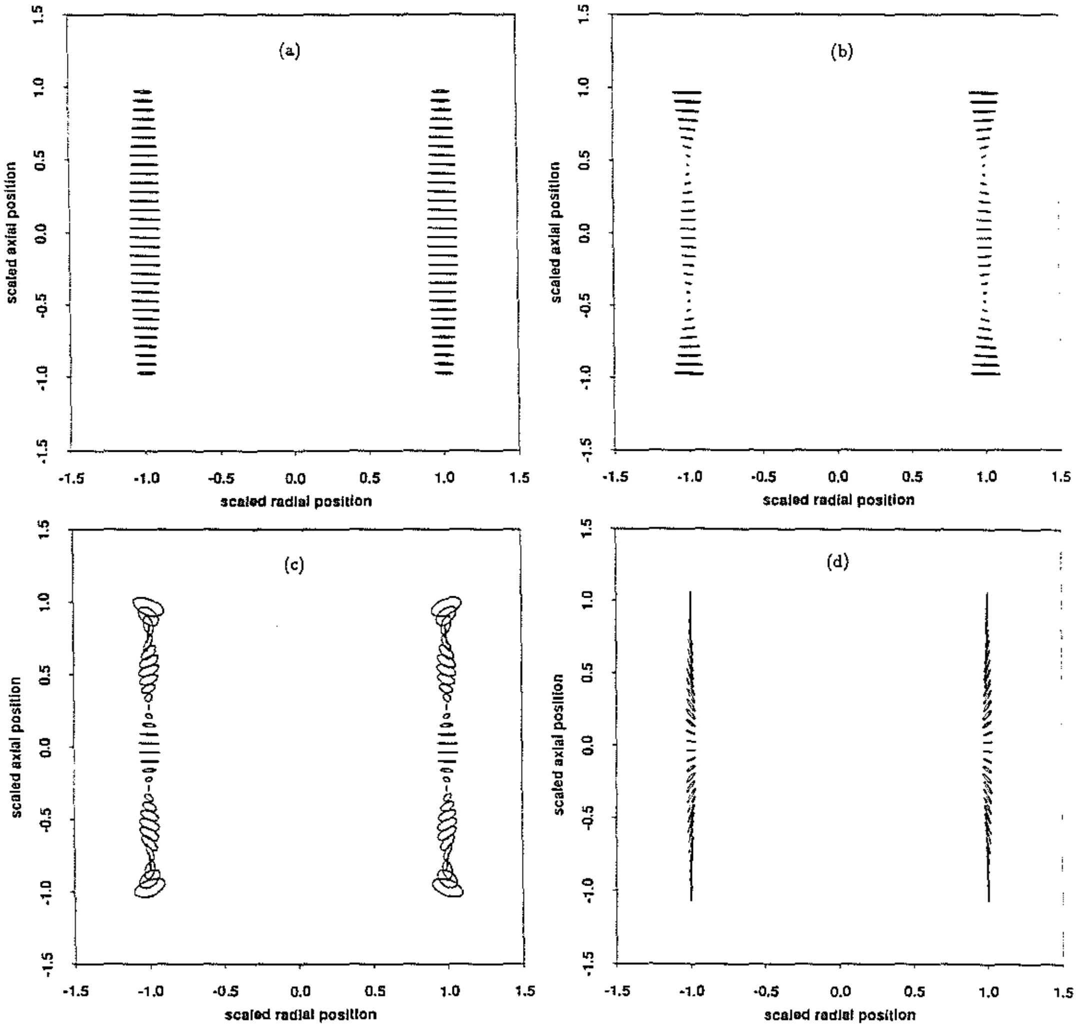

Figure 12: Particle paths for PZT-5 cylinder in oil. (a) Barrel mode. (b) First radial mode. (c) Second radial mode. (d) Length mode.

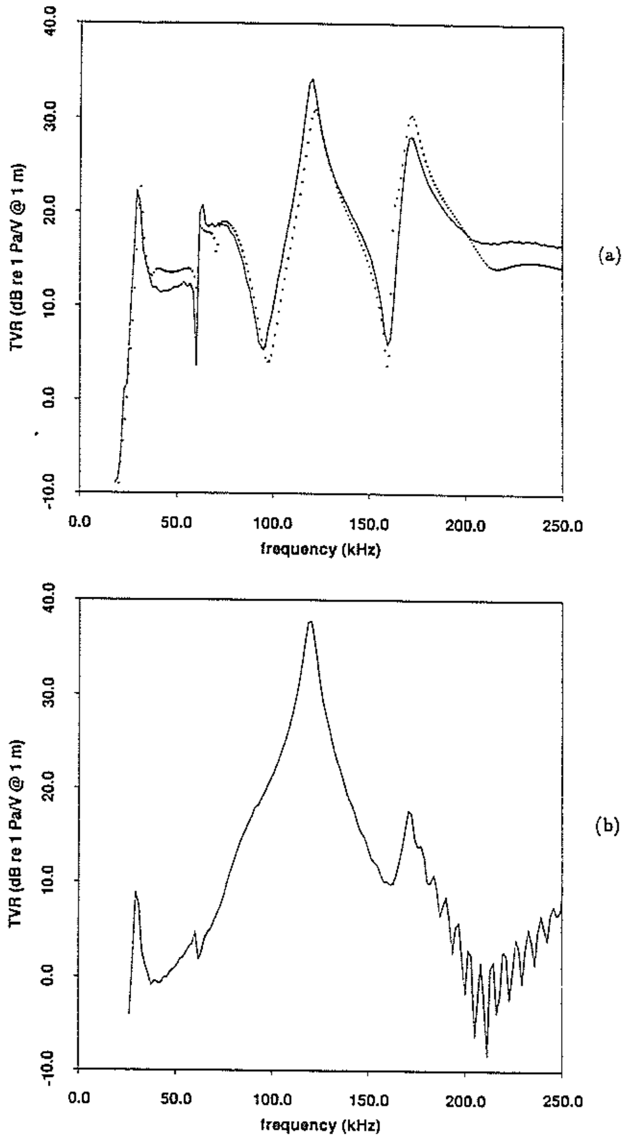

Figure 13: Finite-difference (solid) and experimental (dotted) TVR curves for PZT-5 cylinder in oil. (a) Broadside. (b) Endfire.

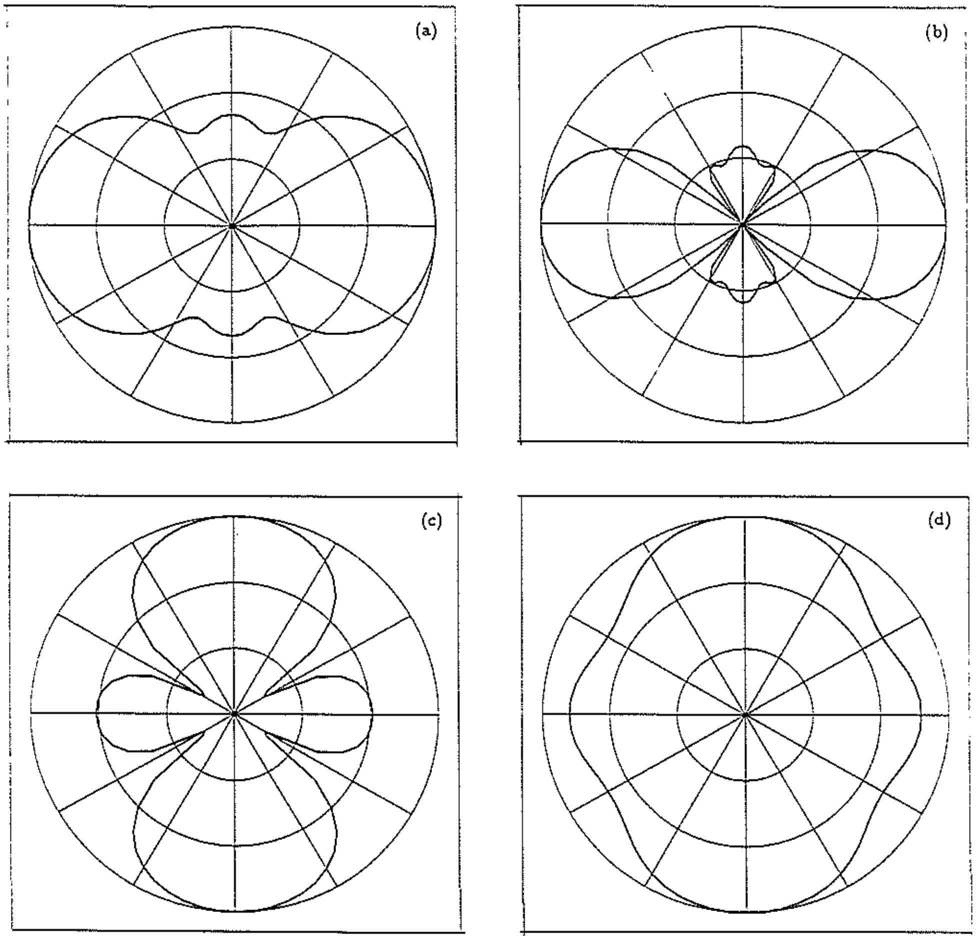

Figure 14: Theoretical far-field radiation patterns. (a) Barrel mode. (b) First radial mode. (c) Second radial mode. (d) Length mode.

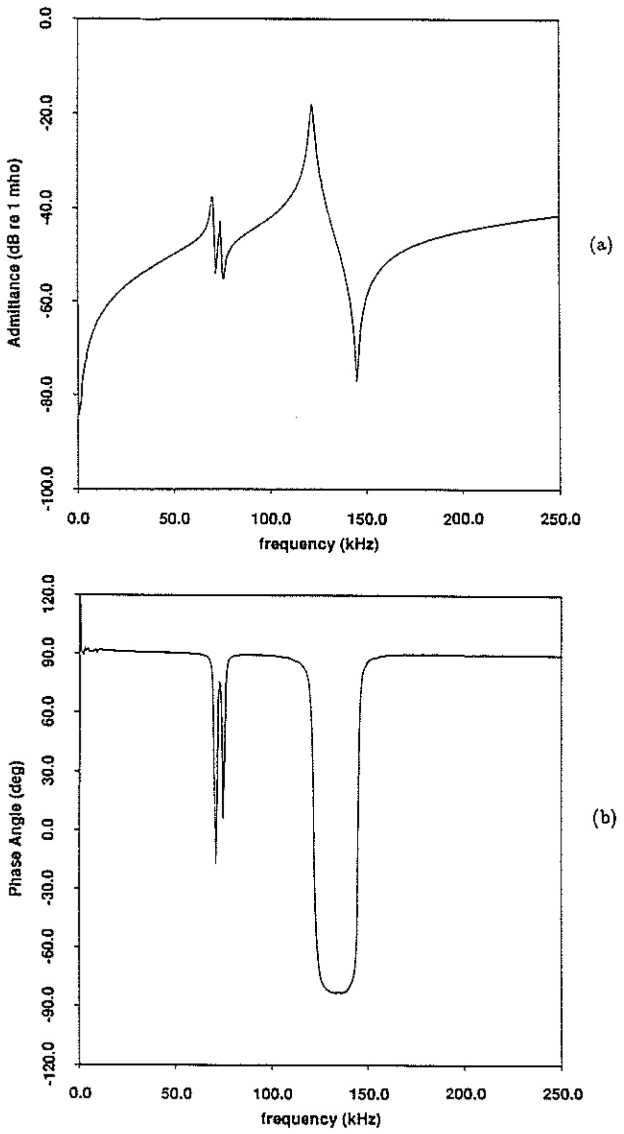

Figure 15: Experimental admittance for PZT-5 cylinder in air. (a) Magnitude. (b) Phase Angle.

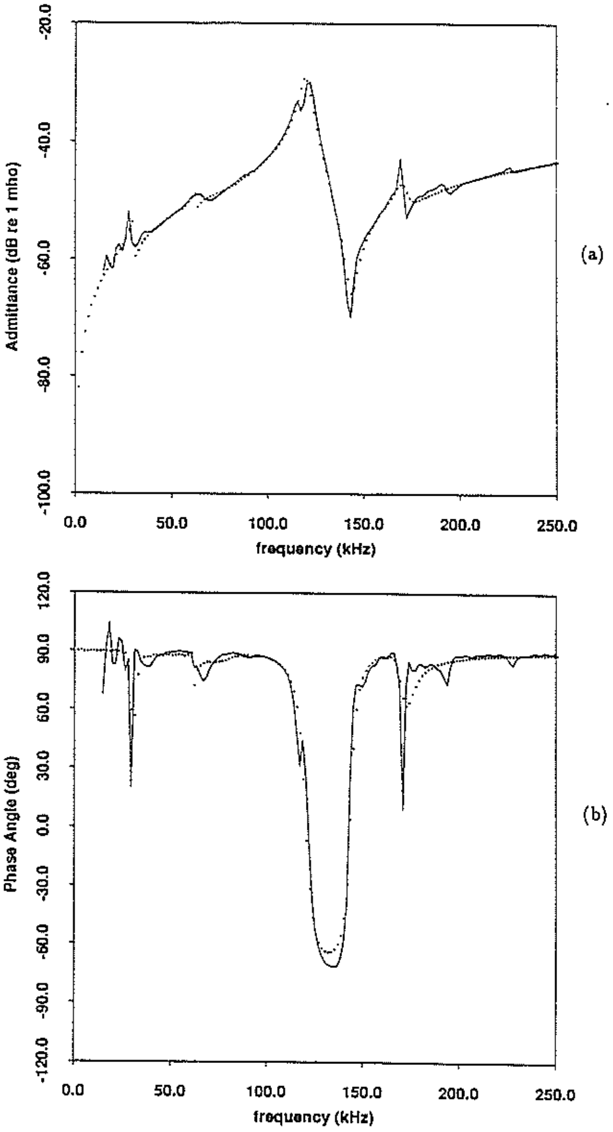

Figure 16: Theoretical admittance for PZT-5 cylinder in free field (borehole) and inside borehole (solid). (a) Magnitude. (b) Phase Angle.

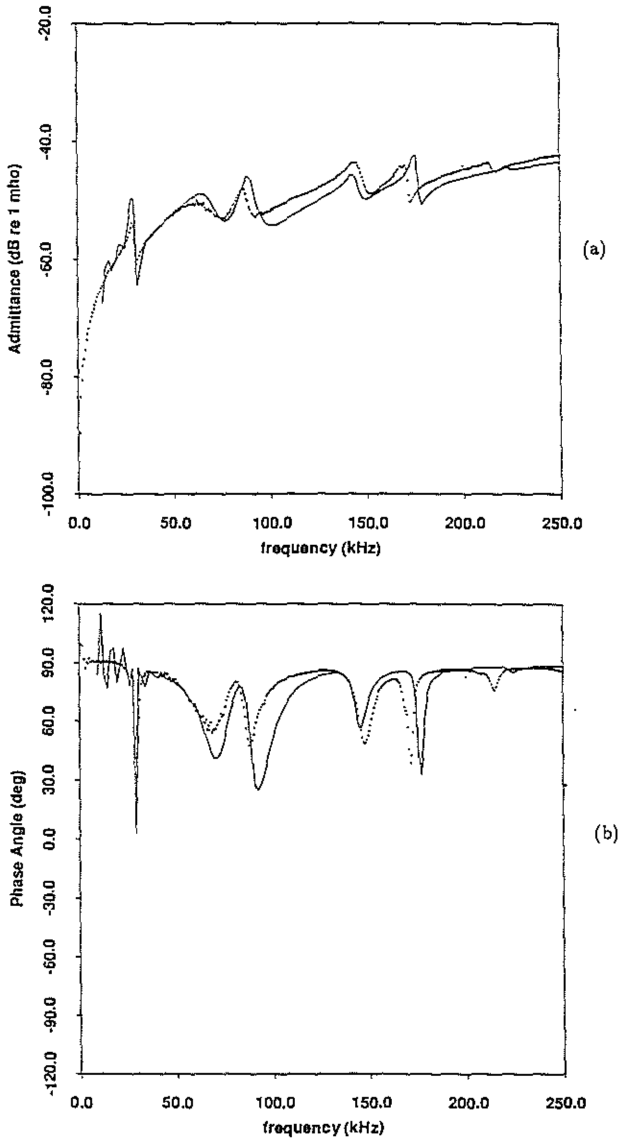

Figure 17: Theoretical (solid) and experimental (dotted) admittance for modified PZT-5 cylinder in oil. (a) Magnitude. (b) Phase Angle.

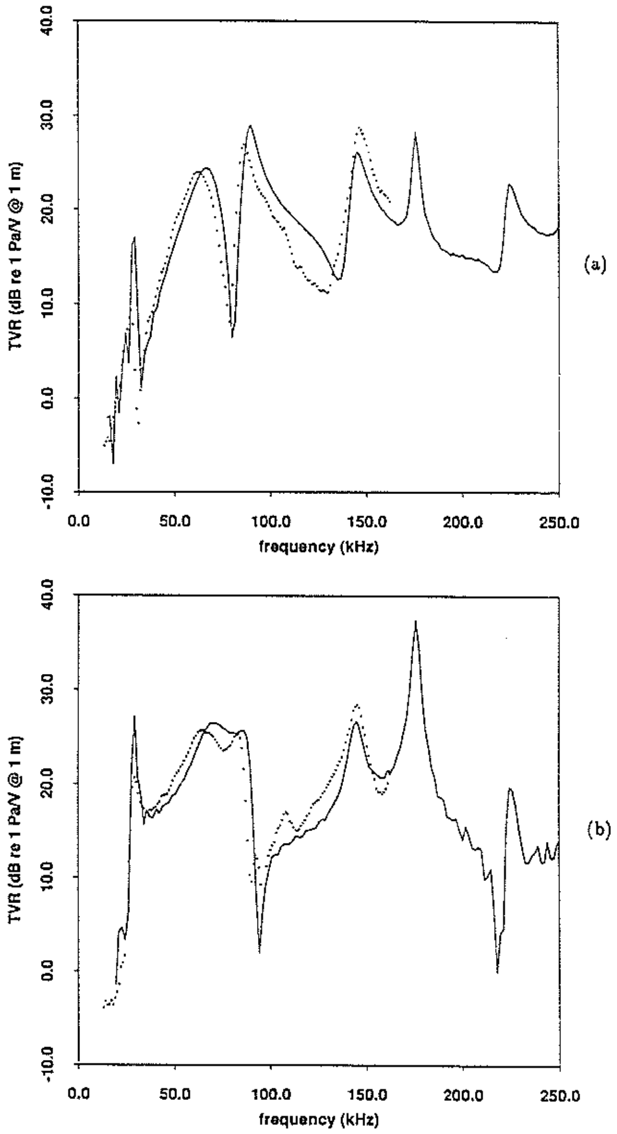

Figure 18: Theoretical (solid) and experimental (dotted) TVR curves. (a) Broadside. (b) Endfire.

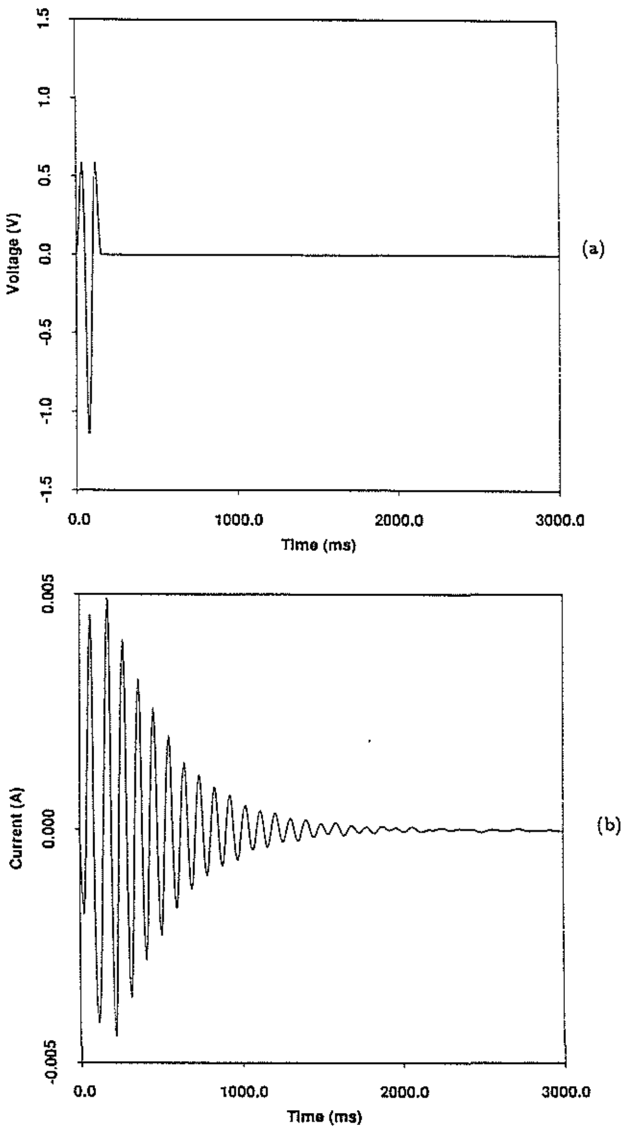

Figure 19: Input-output waveforms in finite-difference simulation of scaled-up PZT-5 cylinder in fluid-filled borehole. (a) Firing voltage. (b) Electric Current.

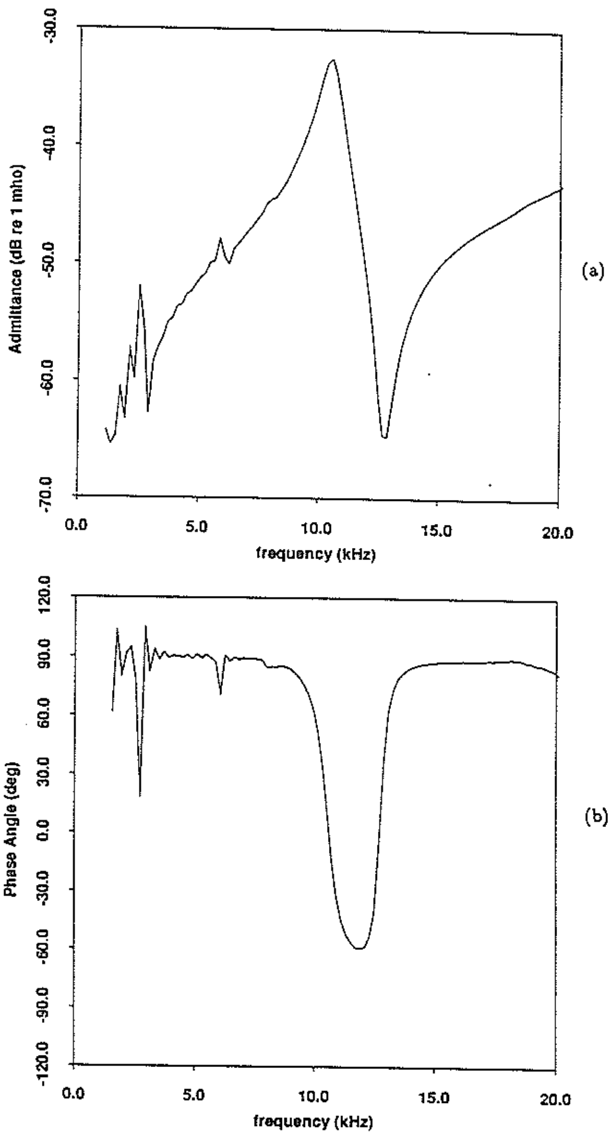

Figure 20: Theoretical admittance of scaled-up PZT-5 cylinder in fluid-filled borehole. (a) Magnitude. (b) Phase Angle.

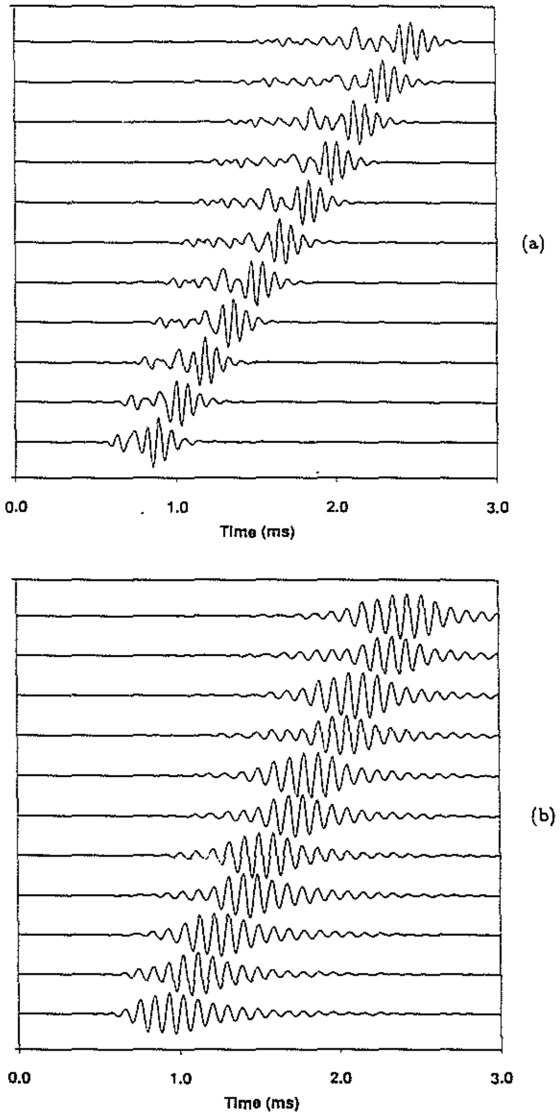

Figure 21: Theoretical waveforms for fluid-filled borehole shown in Figure 4. (a) Excitation by point source. (b) Excitation by PZT-5 cylinder.